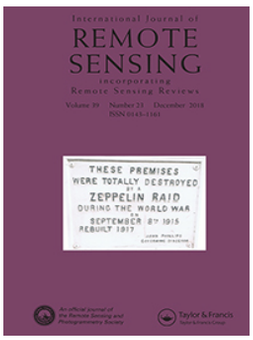

Taylor & Francis
Taylor & Francis Group

International Journal of Remote Sensing

ISSN: 0143-1161 (Print) 1366-5901 (Online) Journal homepage: https://www.tandfonline.com/loi/tres20

Mapping daily leaf area index at 30 m resolution over a meadow steppe area by fusing Landsat, Sentinel-2A and MODIS data

Zhenwang Li, Chengquan Huang, Zhiliang Zhu, Feng Gao, Huan Tang, Xiaoping Xin, Lei Ding, Beibei Shen, Jinxun Liu, Baorui Chen, Xu Wang & Ruirui Yan

To cite this article: Zhenwang Li, Chengquan Huang, Zhiliang Zhu, Feng Gao, Huan Tang, Xiaoping Xin, Lei Ding, Beibei Shen, Jinxun Liu, Baorui Chen, Xu Wang & Ruirui Yan (2018) Mapping daily leaf area index at 30 m resolution over a meadow steppe area by fusing Landsat, Sentinel-2A and MODIS data, International Journal of Remote Sensing, 39:23, 9025-9053, DOI: 10.1080/01431161.2018.1504342

To link to this article: https://doi.org/10.1080/01431161.2018.1504342

INTERNATIONAL JOURNAL OF REMOTE SENSING
2018, VOL. 39, NO. 23, 9025–9053
https://doi.org/10.1080/01431161.2018.1504342

Taylor & Francis
Taylor & Francis Group

Mapping daily leaf area index at 30 m resolution over a meadow steppe area by fusing Landsat, Sentinel-2A and MODIS data

Zhenwang Li [a,b], Chengquan Huang [b], Zhiliang Zhu [c], Feng Gao[d], Huan Tang[e], Xiaoping Xin[a], Lei Ding[a], Beibei Shen[a], Jinxun Liu[f], Baorui Chen[a], Xu Wang[a] and Ruirui Yan[a]

[a]National Hulunber Grassland Ecosystem Observation and Research Station, Institute of Agricultural Resources and Regional Planning, Chinese Academy of Agricultural Sciences, Beijing, China; [b]Department of Geographical Sciences, University of Maryland, College Park, MD, USA; [c]The Earth Resources Observation Systems Center, United States Geological Survey, Reston, VA, USA; [d]Hydrology and Remote Sensing Laboratory, USDA-ARS, Beltsville, MD, USA; [e]School of Civil Engineering and Architecture, Tongling University, Tongling, Anhui, China; [f]Western Geographic Science Center, United States Geological Survey, Menlo Park, CA, USA

ABSTRACT

The leaf area index (LAI) is a key vegetation canopy structure parameter and is closely associated with vegetation photosynthesis, transpiration, and energy balance. Developing a landscape-scale LAI dataset with a high temporal resolution (daily) is essential for capturing rapidly changing vegetation structure at field scales and supporting regional biophysical modeling efforts. In this study, two daily 30 m LAI time series from 2014 to 2016 over a meadow steppe site in northern China were generated using a spatial and temporal adaptive reflectance fusion model (STARFM) combined with an LAI retrieval radiative transfer model (PROSAIL). Gap-filled Landsat 7, Landsat 8 and Sentinel-2A surface reflectance (SR) images were used to generate fine-resolution LAI maps with the PROSAIL look-up table method. Two daily 500 m moderate-resolution imaging spectroradiometer (MODIS) LAI product-the existing MCD15A3H LAI product and one was generated from the MCD43A4 SR product and the PROSAIL model, were used to provide temporally continuous LAI variations. The STARFM model was then used to fuse the fine-resolution LAI maps with the two 500 m LAI products separately to generate two daily 30 m LAI time series. Both results were assessed for three types of pasture (mowed pasture, grazing pasture, and fenced pasture) using ground measurements from 2014–2015. The results showed that the PROSAIL-generated LAI maps all exhibited a high accuracy, and the root mean squared errors (RMSEs) for the Landsat 7 LAI and Landsat 8 LAI compared to the ground-measured LAI were 0.33 and 0.28 respectively. The Landsat LAI maps also showed good agreement and similar spatial patterns with the Sentinel-2A LAI with mean differences between ± 0.5. The MCD43A4_PROSPECT LAI product exhibited similar seasonal

ARTICLE HISTORY
Received 31 January 2018
Accepted 8 July 2018

CONTACT Chengquan Huang cqhuang@umd.edu Department of Geographical Sciences, University of Maryland, College Park, MD 20742, USA; Zhiliang Zhu zzhu@usgs.gov United States Geological Survey, Reston, VA 20192, USA; Xiaoping Xin Xinxinxiaoping@caas.cn National Hulunber Grassland Ecosystem Observation and Research Station, Institute of Agricultural Resources and Regional Planning, Chinese Academy of Agricultural Sciences, Beijing 100081, China

variability to the ground measurements and to the Landsat and Sentinel-2A LAIs, and these data are also smoother and contain fewer noisy points than the gap-filled MCD15A3H LAI product. Compared to the ground measurements, the daily 30 m LAI time series fused from the fine-resolution LAI maps and PROSPECT generated MODIS LAI product demonstrated better performance with an RMSE of 0.44 and a mean absolute error (MAE) of 0.34, which is an improvement from the LAI time series fused from the fine-resolution LAI maps and the existing MCD15A3H LAI product (RMSE of 0.56 and MAE of 0.42). The latter dataset also exhibited abnormal temporal fluctuations, which may have been caused by the interpolation method. The results also demonstrated the very good performance of the STARFM model in grazing and mowed pasture with homogeneous surfaces compared to fenced pasture with smaller patch sizes. The Sentinel-2A data offers increased landscape vegetation observation frequency and provides temporal information about canopy changes that occur between Landsat overpass dates. The scheme developed in this study can be used as a reference for regional vegetation dynamic studies and can be applied to larger areas to improve grassland modeling efforts.

1 Introduction

The structural and functional attributes of vegetation canopies vary with the vegetation types, phenological stages, microclimatic conditions, nutrient dynamics, land management, and many other factors (Asner, Scurlock, and Hicke 2003). The leaf area index (LAI), which is defined as the one-sided green leaf area per unit ground area (Chen and Black 1992), is a key parameter that indicates the integrated effects of these factors. Values of LAI are closely associated with vegetation photosynthesis, transpiration, and energy balance (Asner, Scurlock, and Hicke 2003; Bonan 1993; Running et al. 1989; Wiegand, Richardson, and Kanemasu 1979). As a key canopy structure parameter, LAIs with both high spatial and high temporal resolution are a required input in a number of productivity, hydrology and energy models to effectively model the within-field vegetation dynamics and provide meaningful information for management strategies (Colombo et al. 2003; Running and Coughlan 1988; Sellers and Schimel 1993; Houborg, McCabe, and Gao 2016). Developing a landscape-scale LAI dataset with a high temporal resolution (daily) is therefore essential for understanding regional vegetation biological and physical processes, initiating ecosystem biogeochemistry models, analyzing regional carbon and production dynamics (Colombo et al. 2003; Running et al. 1999; Yin et al. 2017), and monitoring vegetation productivities under different management strategies.

To meet these demands, several global LAI products have been produced from remote sensing data obtained from different satellite sensors, such as the copernicus global land service (CGLS) and the carbon cycle and change in land observational products from an ensemble of satellites (CYCLOPES) LAI products, which are generated from the VEGETATION and project for on-board autonomy-Vegetation (PROBA-V) sensors aboard the systeme probatoire d'observation de la terre (SPOT) satellites (Baret et al. 2007, 2013) and the moderate-resolution imaging spectroradiometer (MODIS) LAI products generated from MODIS sensors aboard the Terra and Aqua satellites (Myneni et al.

2002; Yang et al. 2006). These products are widely used in a broad range of studies of agriculture, ecology, carbon cycling, and climate (Ganguly et al. 2012). Although these sensors can provide daily global observations that are valuable for monitoring vegetation dynamics, the coarse-spatial resolution (250–1000 m) of these sensors and their products is often inadequate for field-scale LAI estimation (Gao et al. 2015; Ganguly et al. 2012). In addition, the products are often composited and updated every 4–10 days to decrease cloud and observation angle interruptions. Finer-resolution (30 m) Landsat series satellite observations have provided better data for deriving landscape-scale modeling inputs since the first launch of these satellite sensors in the 1970s (Huang et al. 2009; Masek et al. 2006; Wulder et al. 2012). The advanced spaceborne thermal emission and reflection radiometer (ASTER) and Sentinel-2 data, which offer a comparable or even higher spatial resolution, became available in 1999 and 2015, respectively, and represent additional data sources that provide more choices for landscape-scale studies (Drusch et al. 2012). However, finer spatial resolutions typically result in smaller image footprints and thereby decrease the revisit time (5–16 days) for observations at the same location. Cloud contamination during the vegetation growing season may further lengthen the revisit interval, which limits the use of these data for capturing rapid surface changes (Coops, Matt Johnson, and White 2006; Ju and Roy 2008; Gao et al. 2015; Gao, Schwaller, and Hall 2006).

Methods combining these two types of satellite images to generate synthesized data with both high spatial resolution and frequent coverage have recently been developed (Zhu et al. 2016; Gao et al. 2015; Li et al. 2017a; Gao, Schwaller, and Hall 2006; Huang and Song 2012; Mingquan et al. 2012; Sedano, Kempeneers, and Hurtt 2014; Huang et al. 2016). Among these methods, the spatial and temporal adaptive reflectance fusion model (STARFM) developed by Gao, Schwaller, and Hall (2006) was the first weighted function-based spatial-temporal image fusion method, and it has been widely used for monitoring seasonal changes in vegetation succession and conditions (Rao et al. 2015; Hilker et al. 2009b; Wang, Gao, and Masek 2014; Gao et al. 2017). The model uses one or two image pairs from Landsat and MODIS to estimate Landsat-resolution images at MODIS acquisition dates. The STARFM model was later improved to study forest disturbances (Hilker et al. 2009a) and heterogeneous regions (Zhu et al. 2010). STARFM was originally used to detect reflectance changes caused by processes such as phenology, but subsequent studies have found this model useful for mapping high-resolution key environmental variables. Researchers used STARFM and a two-source energy balance model to estimate daily field-scale evapotranspiration at field to continental scales (Anderson et al. 2011; Sun et al. 2017; Yang et al. 2017). Weng, Peng, and Gao (2014) improved STARFM to predict the daily land surface temperature (LST) at a 120 m resolution by blending Landsat thematic mapper (TM) and MODIS LST data. Gao et al. (2017) generated daily 30 m surface reflectance (SR) imagery using the STARFM approach in central Iowa, USA from 2001–2015 and produced 30 m crop phenology maps. Houborg, McCabe, and Gao (2016) developed a multi-scale spatio-temporal enhancement method for medium-resolution LAI (STEM-LAI) based on STARFM that is used to downscale the 8-day MODIS LAI products to the resolution of the 4-day Landsat-scale LAI dataset. The STEM-LAI results showed high performance at the test site; however, reliable downscaling of MODIS LAIs to the Landsat scale requires sufficient homogeneous samples at the MODIS resolution, which is a significant challenge for the

method. Additionally, directly interpolating 8-day MODIS LAI products to daily time steps will add uncertainty to the results.

An accurate estimation of vegetation LAI from the two types of satellite data is one key issue to generate high-quality spatial-temporal LAI datasets. Although MODIS and the first version of the Geoland2 products (GEOV1) LAI products are freely available, the comparatively long composite time interval (4–16 days for MODIS and 10 days for GEOV1) make them unsuitable for daily LAI mapping. In addition, the MODIS LAI products were validated with different performance in different vegetation biomes (Li et al. 2015; Yan et al. 2016b). A number of LAI prediction methods have been developed from remotely sensed data, which can be generally grouped in two categories: the statistical and physical (Baret and Buis 2008; Verrelst et al. 2015). The empirical statistical methods that builds relationships between LAI and a spectral observation or a combination of spectral observations (vegetation indices, VIs) has been widely used due to its simplicity and relatively good performance; however, such approaches are site-, time-, sensor-, and biome-specific and their application is constrained by surface representativeness, sensor spectral information and sun position as well as viewing geometry (Weiss and Baret 1999; Verrelst et al. 2008, 2010; Tao et al. 2016; Gao et al. 2012). The physically-based radiative transfer models are based on a rigorous physical description of the interactions between electromagnetic radiation, canopy elements and the underlying soil surface (Dorigo et al. 2007). They can simulate a great variety of conditions in terms of vegetation type and surface characteristics as well as sensor acquisition geometry, thus the approaches are generic and therefore generally applicable. However, the physically-based approaches are computationally demanding and ill-posed which may lead to instability in the results (Combal et al. 2003; Pasolli et al. 2015). To cope with these issues, some restrictions were proposed to constrain the inversion process, these involve reducing the look-up table (LUT) dimensions (Gastellu-Etchegorry, Gascon, and Estève 2003), the use of prior knowledge (Combal et al. 2003), and the use of multiple solutions of LUT inversion (Darvishzadeh et al. 2008).

In this study, we developed a scheme to generate two daily 30m LAI time series over a meadow steppe site in northern China by fusing Landsat, Sentinel-2A, and MODIS LAI data. The PROSAIL model was used to generate LAI maps from Landsat and Sentinel-2A SR images and the MCD43A4 nadir bidirectional reflectance distribution function adjusted reflectance (NBAR) product, and the STARFM algorithm was then used to combine the spatio-temporal characteristics of the fine-resolution Landsat and Sentinel-2A LAI maps and the temporally continuous PROSAIL generated MODIS LAI product (MCD43A4_PROSPECT_STARFM LAI). To assess the spatio-temporal performance of the MCD43A4_PROSPECT_STARFM LAI data, a second daily 30 m LAI dataset was generated by fusing the finer-scale LAI maps with the existing MCD15A3H LAI product (MCD15A3H_STARFM LAI). The results of the two LAI time series were then compared and validated using ground measurements. The objectives of this study are (1) to assess the ability of the PROSAIL model to generate grassland LAIs from satellite data with different spatial resolutions; (2) to compare the spatio-temporal consistency of Sentinel-2A and Landsat data in the estimation of grassland LAIs; (3) to assess the ability of our scheme to generate daily 30 m LAI datasets; and (4) to analyze the spatio-temporal variability of the LAIs in different pasture types and its response to climate factors.

2 Materials

2.1 *Study site*

Hulunber city (Inner Mongolia Autonomous Region, China) has the most complete and best-preserved natural temperate meadow steppe on the Eurasian continent and has an amazing abundance of species with high economic and ecological value (Li et al. 2016). The study was conducted at an experimental site at the Hulunber grassland ecosystem observation and research station (Hulunber station, 49°20′24″ N, 119°59′44″ E), which is located in the middle of the Hulunber meadow steppe (Figure 1). The site covers an area of 4 km× 4 km and has a homogeneous surface. *Leymus chinensis* and *Stipa baicalensis* are the two dominant grass species, and a small river (covering approximately 0.30 km^2) is located in the southeast part of the study area. The region is characterized by a semi-arid inland climate with an annual mean precipitation of 350 mm–400 mm and annual mean temperatures ranging from −3°C to 1°C. The average elevation at the site is 650 m. The growing season is approximately 140 days long (May to September) (Tang et al. 2015b; Li et al. 2015). Three pasture types exist in the study site (Wu et al. 2015): open grazing pasture (6.18 km^2), which feeds cattle from June to September; mowed pasture (9.15 km^2), which is used for silage (harvested once or twice in August) and is fenced throughout the year to prevent cattle grazing; and fenced pasture (0.37 km^2), which is

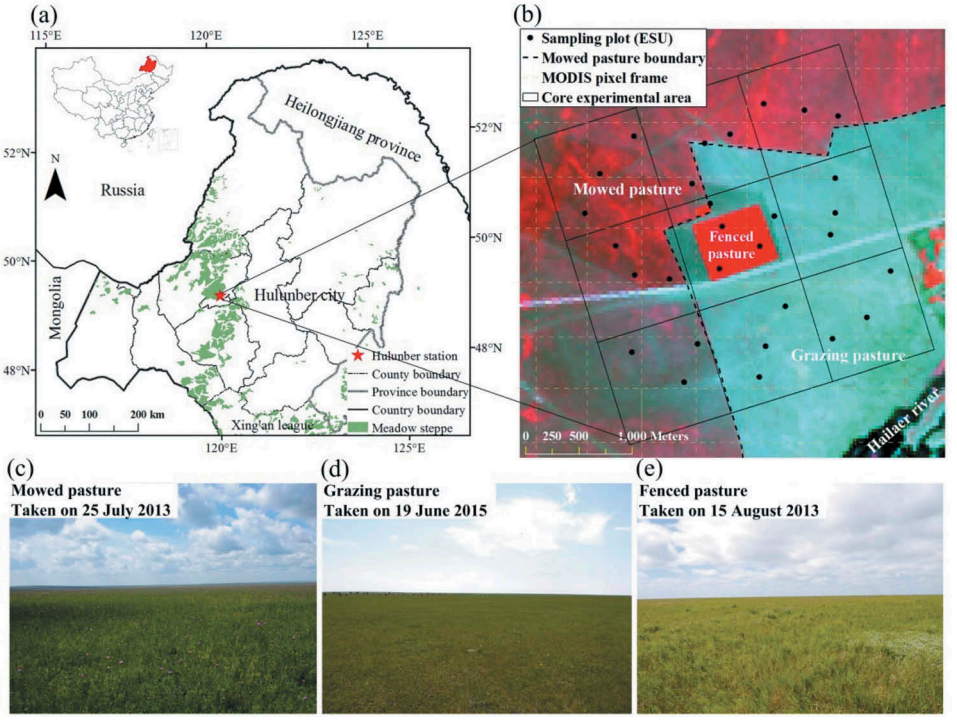

Figure 1. (a) The geographic location of Hulunber station. (b) The experimental site and sampling plots (background: Landsat-8 operational land imager (OLI) false-color composite image (5, 4, and 3) from 5 July 2015). (c) Picture of mowed pasture in the site. (d) Picture of grazing pasture in the site. (c) Picture of fenced pasture in the site.

protected from grazing and harvesting. A wildfire occurred in the fenced pasture on April 2015, and the dead grass that had accumulated over the previous ten years was removed.

2.2 *Field measurements*

Field sampling was performed during the growing seasons (June to August) of 2014 and 2015 in the core experimental area (3 km× 3 km) of the site. A two-scale sampling strategy (site scale and image pixel scale) designed by the VALERI project (De Kauwe et al. 2011; Philippe Rossello 2007) was adopted to collect the grass LAI. A total of 29 elementary sampling units (ESUs, 30 m × 30 m) were chosen at the site (Figure 1). A more detailed sampling protocol for this site has been described previously (Li et al. 2014). Each ESU was located with a global positioning system (GPS) receiver that was accurate to 2 m, which ensured that the measurements for each campaign were collected at the same location. The effective LAI was measured using an LAI-2200C plant canopy analyzer (Li-Cor, Lincoln, NE, USA) with a 270° view cap. At each ESU, the effective LAI was measured at five points arranged in a 'cross' pattern, and the five LAI values were then averaged to calculate a mean value to obtain a representative remote sensing pixel value. During 14 field campaigns at the experimental site, a total of 342 LAI ESU measurements were collected; the statistics of the measured LAIs are shown in Table 1.

Other grass biophysical parameters used in the PROSAIL model were also randomly collected from the three pasture types during each field campaign. The leaf chlorophyll concentration (LCC) was collected and calculated using a SPAD-502 chlorophyll meter (Minolta Corporation, Ltd., Osaka, Japan), the leaf inclination angle was measured using a protractor, and the dry matter content and water content were collected by the harvest method and dried in an oven at 85°C.

2.3 *Satellite data*

To increase the temporal frequency of the ground observations at finer resolutions, Landsat 7 enhanced thematic mapper plus (ETM+) images, Landsat 8 operational land imager (OLI) images, and Sentinel-2A MultiSpectral Instrument (MSI) images were used

Table 1. Descriptive statistics of the measured leaf area index (LAI) dataset.

Date	Number of sampling unit	Mean	Minimum	Maximum	Standard deviation
31 May 2014	26	1.15	0.61	1.69	0.31
23 June 2014	24	1.47	0.55	1.86	0.34
1 July 2014	26	2.15	0.81	3.22	0.63
4 July 2014	23	1.76	0.42	2.81	0.67
11 July 2014	25	1.91	0.65	2.79	0.73
28 July 2014	26	1.82	0.69	2.75	0.78
3 August 2014	22	1.83	1.03	2.90	0.65
18 August 2014	23	1.30	0.84	2.00	0.31
19 June 2015	25	1.26	0.77	1.81	0.37
30 June 2015	22	1.20	0.41	2.19	0.57
5 July 2015	23	1.34	0.51	2.76	0.67
7 July 2015	25	1.18	0.51	2.01	0.56
11 August 2015	26	1.47	0.69	3.40	0.74
20 August 2015	26	1.28	0.76	2.32	0.41
Total	342	1.45	0.41	3.40	0.65

in this study. Higher-level Landsat surface reflectance data products from path 123, row 26 from early May to the end of October from 2014 to 2016 were ordered and downloaded from the USGS Earth Explorer website (http://earthexplorer.usgs.gov/). Landsat data are routinely corrected radiometrically and geometrically (level 1G) by the USGS Earth Resources Observation and Science (EROS) Center. A terrain correction (Level 1T) is applied using a digital elevation model (DEM) and ground control points. The Landsat 7 ETM+ surface reflectance product is atmospherically corrected using the second simulation of a satellite signal in the solar spectrum (6S) radiative transfer model (Masek et al. 2006). The Landsat 8 surface reflectance data are generated from the Landsat surface reflectance code (LaSRC), and atmospheric correction was conducted using a refined 6S radiative transfer model (Vermote et al. 2016). Because the short wave infrared (SWIR) band between 1.55–1.75 nm is susceptible to atmospheric aerosols and water vapor, the SWIR1 band (band 5 for Landsat 7 ETM+ and band 6 for Landsat 8 OLI) was abandoned in this study after the reflectance was checked (Li, Xin, et al. 2017). The 30 m resolution spectral blue, green, red, near-infrared (NIR) and SWIR2 bands (bands 1, 2, 3, 4 and 7 for Landsat 7 ETM+ images and bands 2, 3, 4, 5 and 7 for Landsat 8 OLI images, respectively) were used for LAI estimation (Landsat LAI). Fifteen cloud-free Landsat scenes over the study site were available during the growing seasons of 2014–2016, including nine Landsat 7 scenes and six from Landsat 8 (Table 2).

The Sentinel-2A MSI sensor acquires 13 spectral bands ranging from the visible and near-infrared (VNIR) to shortwave infrared (SWIR) wavelengths along a 290-km orbital swath. The spatial resolutions of these bands range from 10 to 60 m, and the minimum revisit time at the equator is 10 days (Drusch et al. 2012). The Sentinel-2A MSI images of the study area were collected and processed on six cloud-free days in 2016. Four scenes (day of year (DOY): 154, 201, 221, and 241) were used for data fusion, and the other two (DOY: 214 and 274) were used to compare the LAI estimation capability with the Landsat data (Table 2). The level 1C top-of-atmosphere (TOA) reflectance data were acquired from the USGS Earth explorer website (http://earthexplorer.usgs.gov/). The data processing included radiometric and geometric corrections along with orthorectification to

Table 2. Spectral bands and acquisition dates of the Landsat ETM+, OLI, Sentinel-2A MSI, and MODIS data used in this study.

Satellite data	Landsat 7 ETM+	Landsat 8 OLI	Sentinel-2A MSI	MODIS
Bands used in this study and their bandwidth (μm)	B1 (0.441–0.514) B2 (0.519–0.601) B3 (0.631–0.692) B4 (0.772–0.898) B7 (2.064–2.345)	B2 (0.452–0.512) B3 (0.533–0.590) B4 (0.636–0.673) B5 (0.851–0.879) B7 (2.107–2.294)	B2 (0.458–0.523) B3 (0.543–0.578) B4 (0.650–0.680) B5 (0.698–0.713) B6 (0.733–0.748) B7 (0.765–0.785) B8a (0.855–0.875) B11 (1.565–1.655) B12 (2.100–2.280)	B3 (0.459–0.479) B4 (0.545–0.565) B1 (0.620–0.670) B2 (0.841–0.876) B5 (1.230–1.250) B6 (1.628–1.652) B7 (2.105–2.155)
Spatial resolution (m)	30	30	10/20	250/500
Acquired date (Juliay day)	2,014,207; 2,014,239; 2,014,287; 2,015,114; 2,015,258; 2,016,165; 2,016,213; 2,016,261; 2,016,277	2,014,119; 2,014,151; 2,015,170; 2,015,186; 2,015,282; 2,016,125	2,016,154; 2,016,201; 2,016,214; 2,016,221; 2,016,241; 2,016,274	2,014,120–290; 2,015,120–290; 2,016,120–290

generate highly accurate geolocated products. The atmospheric, terrain and cirrus corrections of the TOA level 1C data were then conducted using the Sen2Cor (Sentinel-2 atmospheric correction) processor integrated with the sentinel application platform (SNAP) toolbox. Only spectral bands with a spatial resolution of 10m or 20m were considered in this study. The 10m resolution spectral blue, green and red bands (bands 2, 3 and 4) and 20m resolution spectral vegetation red edge, narrow NIR, SWIR1 and SWIR2 bands (bands 5, 6, 7, 8A, 11 and 12) were used for the LAI estimation (Sentinel LAI). Before the LAI estimation, all of the bands were resampled to a 20 m spatial resolution.

The daily MCD43A4 NBAR products of tile h25v04 from 2014 to 2016 were acquired from the Earthdata search client website of the Earth observing system data and information system (EOSDIS) (https://earthdata.nasa.gov/). The MCD43A4 product provides 500m NBAR data and is computed for each of the MODIS spectral bands (1–7) at local solar noon for the day of interest using the bidirectional reflectance distribution function to model the values as if they were collected from a nadir view (Schaaf and Wang 2015). All seven bands were used to generate coarse-resolution LAI maps (MCD43A4_PROSPECT LAI). In addition, the MODIS 4-day LAI product (MCD15A3H LAI) at a 500 m spatial resolution was fused with the Landsat and Sentinel LAI data in the STARFM to generate a 4-day 30 m LAI dataset, which was then interpolated to daily time steps using a cubic spline function.

3 Methods

In this study, three major components were included in the processing stream: the PROSAIL model, which was applied to the Landsat 7, Landsat 8, Sentinel-2A and MODIS SR imagery to retrieve LAIs at different spatial and temporal resolutions; STARFM, which was used to fuse the data; and the gap-filling procedure applied to the Landsat 7 SLC-off ETM+ images to fill image gaps prior to LAI retrieval and fusion. The processing flow chart is shown in Figure 2. During the LAI retrieval process, the 30 m gap-filled Landsat 7, 30 m Landsat 8, 20 m Sentinel-2A SR data and 500 m MCD43A4 NBAR data were input into the PROSAIL model, and the retrieved LAI maps were then reprojected and resampled to the same image size and pixel size (30 m). The data fusion process used STARFM with a single Landsat (Sentinel-2A)-MODIS pair to predict nearby dates of similar phenological phases. Before conducting the data fusion process, the LAI maps retrieved from the Landsat and Sentinel-2A images were compared to check their spatio-temporal consistency. Two daily 30 m LAI time series were generated: one was fused from the PROSAIL-generated Landsat, Sentinel-2A and daily MCD43A4_PROSPECT LAI maps (MCD43A4_PROSPECT_STARFM LAI), and the other was fused from the PROSAIL-generated Landsat and Sentinel-2A LAI maps and the existing 4-day MCD15A3H LAI product (MCD15A3H_STARFM LAI); the latter was then interpolated to a daily timestep by fitting a cubic spline function.

3.1 *PROSAIL*

PROSAIL is a radiative transfer model that combines the PROSPECT leaf optical properties model (Jacquemoud and Baret 1990) and scattering by arbitrarily inclined leaves (Verhoef 1984, 1985). The model has been used to study plant canopy spectral and directional reflectance in the solar domain (Jacquemoud et al. 2009). The model can also be used to

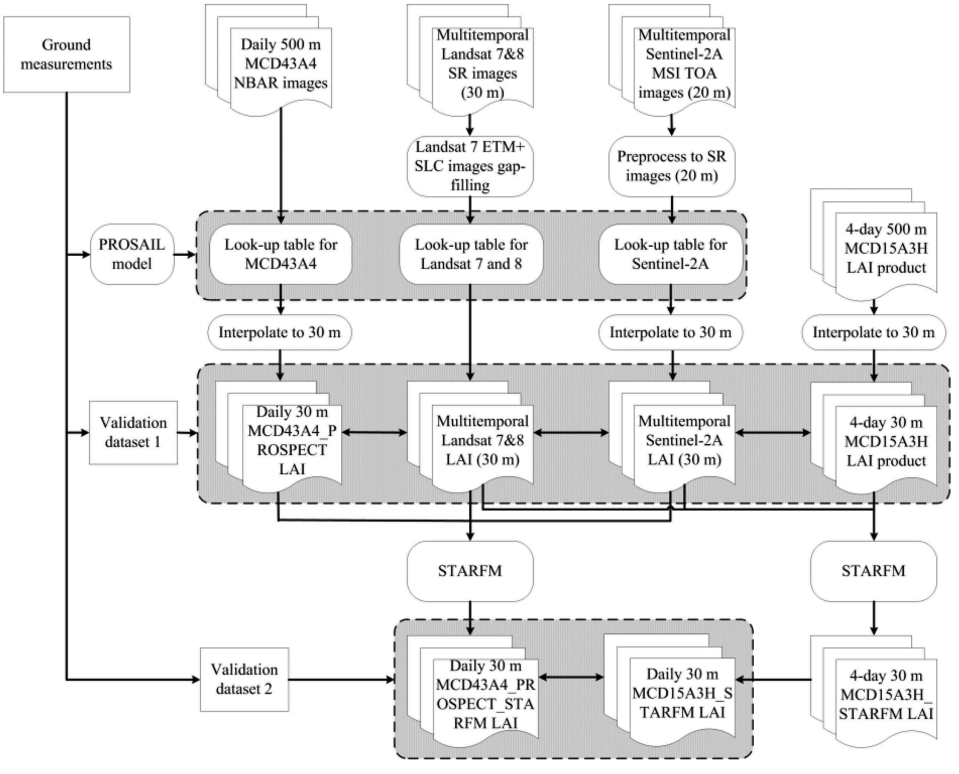

Figure 2. Flowchart of the process used to estimate the daily 30 m LAI in this study.

develop new methods for the retrieval of vegetation biophysical properties (e.g., LAI and canopy chlorophyll contents) (Darvishzadeh et al. 2008; Goel 1988; Jacquemoud et al. 1995). The PROSPECT5 model simulates leaf directional-hemispherical reflectance and transmittance over the solar spectrum from 400 nm to 2500 nm (Jacquemoud and Baret 1990; Jacquemoud et al. 1996; Feret et al. 2008). The model considers a leaf as one or several absorbing plates with rough surfaces that causeisotropic scattering and was developed from the plane-parallel model (Allen et al. 1969). The absorption of light is assumed to be entirely caused by leaf biochemical contents (chlorophyll, water, and dry matter). Four input parameters are required: the leaf structural parameter (N), the leaf chlorophyll a + b concentration (LCC), the dry matter content (C_m), and the equivalent water thickness (C_w). The SAIL model is an extended one-dimensional model that simulates the bidirectional reflectance factor of turbid medium plant canopies (Verhoef 1984, 1985; Schaepman-Strub et al. 2006). The model treat the canopy as a horizontally homogeneous and semi-infinite layer that consists of small vegetation elements, which act as absorbing and scattering particles of a given geometry and density (Verhoef et al. 2007). 4SAIL is a numerically robust and speed-optimized version of the SAIL model (Verhoef et al. 2007). The coupling of the PROSPECT5 and 4SAIL models simply consists of passing the output leaf reflectance and transmittance of the PROSPECT5 model into the 4SAIL model to simulate the entire spectrodirectional canopy reflectance field (Jacquemoud et al. 2009). In addition to the leaf reflectance and transmittance, the 4SAIL model requires eight input

parameters: the sun zenith angle (θ_s), view zenith angle (θ_v), sun-sensor azimuth angle (φ), fraction of diffuse incoming solar radiation (f_{skyl}), soil scaling factor (α_{soil}), LAI, average leaf angle (ALA), and hot spot size parameter (H).

The LUT-based inversion method was used in this study to retrieve the grassland LAI from the Landsat, Sentinel-2A and MODIS SR images. This method permits a global search in the LUT for the best solution by minimizing the summed differences between the simulated and measured reflectances. The ranges and distributions of the PROSAIL input variables used to build the LUT, which were obtained from field measurements and the literature (Pasolli et al. 2015; Darvishzadeh et al. 2008), are shown in Table 3. Four LUTs were built for the four satellite datasets separately using the same leaf, canopy and soil parameters but different band and angle information. Since the sum of all of the combinations led to an unrealistically large number of simulations, 100,000 parameter combinations were randomly generated for each LUT to improve the computational efficiency. After several trials using field data, the addition of 2% Gaussian noise to the cost function (root mean squared error, RMSE) resulted in better performance and was used in our LUT inversion process. The LUT generation and LAI inversion processes were conducted in the automated radiative transfer models operator (ARTMO) software package (Verrelst, Romijn, and Kooistra 2012).

3.2 *Spatial and Temporal Adaptive Reflectance Fusion Model (STARFM)*

The STARFM algorithm, which was developed by Gao, Schwaller, and Hall (2006), was originally designed to generate daily surface reflectance data at the Landsat resolution by fusing temporally sparse Landsat imagery with daily but coarse-spatial resolution MODIS imagery. This algorithm has also demonstrated utility in fusing higher-order satellite products with similar instruments (Yang et al. 2017; Li et al. 2017b). In STARFM, for each MODIS and Landsat image pair, a moving search window method is used to identify similar neighboring pixels using a defined threshold between the central pixel and the neighboring pixels. The predicted value for the central pixel $L\left(x_{\frac{w}{2}}, y_{\frac{w}{2}}, t_0\right)$ on date t_0 is computed with a weighting function from spectrally similar neighboring pixels within a specified search window:

Table 3. Specific ranges for the input parameters used to generate the LUT using PROSAIL.

Model parameter	Abbr.	Unit	Value/range	Step
PROSPECT				
Leaf structural parameter	N	No dimension	1.5–2.0	0.1
Leaf chlorophyll content	LCC	μg cm^{-2}	35–70	5
Equivalent water thickness	C_w	g cm^{-2}	0.006–0.045	0.002
Leaf dry matter content	C_m	g cm^{-2}	0.005–0.03	0.0015
4SAIL				
Leaf area index	LAI	No dimension	0.1–5	0.1
Average leaf angle	ALA	Degree	40–70	5
Hot spot size parameter	H	No dimension	0.05–0.3	0.1
Fraction of diffuse incoming solar radiation	f_{skyl}	No dimension	0.1	
Soil scaling factor	α_{soil}	No dimension	0–1	0.1
Sun zenith angle	θ_s	Degree	Value acquired from image metadata	
View zenith angle	θ_v	Degree	Value acquired from image metadata	
Sun-sensor azimuth angle	φ	Degree	0	

$$L\left(x_{\frac{w}{2}}, y_{\frac{w}{2}}, t_0\right) = \sum_{i=1}^{w}\sum_{j=1}^{w}\sum_{k=1}^{n} W_{ijk} \times \left(M(x_i, y_j, t_0) + L(x_i, y_j, t_k) - M(x_i, y_j, t_k)\right) \quad (1)$$

where w is size of the the moving window, $\left(x_{\frac{w}{2}}, y_{\frac{w}{2}}\right)$ is the center pixel of the moving window, $\left(x_i, y_j\right)$ is the pixel location, $M\left(x_i, y_j, t_0\right)$ is the MODIS pixel at the predicted time t_0, $M\left(x_i, y_j, t_k\right)$ is the value of the MODIS pixel at time t_k, $L\left(x_i, y_j, t_k\right)$ is the value of the Landsat pixel at time t_k, and W_{ijk} is the weighting factor that determines the contribution of a spectrally similar pixel within the moving window to the estimation of the center pixel value. In our LAI fusion process, STARFM uses the weighting function derived from the Landsat (or Sentinel-2A) and MODIS LAI retrieved on the same date. The 30 m LAI values were predicted for the dates when MODIS LAI data are available.

3.3 *Gap-filling methods*

The scan-line corrector (SLC) of the Landsat 7 ETM+ sensor failed after 2003, resulting in striped gaps in all but the center of each scene (Arvidson et al. 2006). Filling the gaps in SLC-off ETM+ images is crucial and necessary to ensuring the optimal spatial coverage and temporal continuity in the fused 30 m daily time series. The geostatistical neighborhood similar pixel interpolator (GNSPI) algorithm developed by Zhu, Liu, and Chen (2012) is used in this study to gap-fill the Landsat 7 SLC-off reflectance data. GNSPI divides the predicted pixel value in the SLC-off data gap into a temporal trend and a residual. The temporal trend is estimated using the neighboring pixels with similar spectral characteristics, and the residual is predicted through an ordinary kriging algorithm. This algorithm has been demonstrated to be superior to existing methods, especially in heterogeneous landscapes (Zhu, Liu, and Chen 2012; Romero-Sanchez et al. 2015). For a more detailed description of the algorithm, please refer to Zhu, Liu, and Chen (2012).

For the 4-day time series MCD15A3H LAI product, a simple gap filling method developed by Xiao et al. (2003) was used to fill in the LAI values of cloudy pixels identified by the product quality control (QC) layer. A three-point time series filter ($X_{(t-1)}$, $X_{(t)}$ and $X_{(t+1)}$) was first selected, and the values of the non-cloudy pixels in this window were used to correct the cloudy pixel. If both the $X_{(t-1)}$ and $X_{(t+1)}$ pixels were cloud-free, the average of $X_{(t-1)}$ and $X_{(t+1)}$ was calculated to replace $X_{(t)}$. If the algorithm did not succeed in a three-point time series filter, the window size was then extended to a five-point time series filter ($X_{(t-2)}$, $X_{(t-1)}$, $X_{(t)}$, $X_{(t+1)}$ and $X_{(t+2)}$) using the same procedure as that for the three-point time series filter.

4 Results

4.1 *Performance of the PROSAIL model*

4.1.1 *Assessing the PROSAIL-generated Landsat LAI maps*

Using the PROSAIL LUT-based inversion method, the LAI maps retrieved from the Landsat and Sentinel-2A images were generated and validated using 121 ground measurements that were collected on the Landsat overpass dates. The scatter plots of

the ground-measured LAI and the PROSAIL- predicted LAIs based on the Landsat images from 2014 to 2015 are shown in Figure 3. The results demonstrated a good correlation between the predicted LAIs and the observed LAIs. The LAI maps retrieved from the Landsat 8 images performed slightly better than those retrieved from Landsat 7, with smaller RMSE and MAE values (0.28 and 0.22, respectively, for the Landsat 8-derived LAIs and 0.33 and 0.28 respectively, for the Landsat 7-derived LAIs), This result may have been caused by the different number of spectral bands input into the PROSAIL LUT.

4.1.2 *Consistency between the PROSAIL-generated Landsat LAI and Sentinel-2A LAI maps*

Both Landsat and Sentinel-2 images have exhibited good performance in generating vegetation biophysical variables (Frampton et al. 2013; Campos-Taberner et al. 2017; Korhonen, Hadi, and Rautiainen 2017). Here, we compare the Sentinel-2A and Landsat images for estimating grassland LAI using the PROSAIL model. Five bands of the Landsat images and nine bands of the Sentinel-2A images were used in the PROSAIL LUT-based inversion method, as described in Section 2.3. The LAI maps retrieved from the two satellite datasets were resampled to the same pixel size (30 m) and then compared to assess their consistency.

The LAI maps generated from the two sensors on nearby overpass dates and their difference maps are shown in Figure 4. Overall, the prediction surfaces were similar in terms of the spatial patterns of the grassland LAIs. The LAI value was highest at the peak of the growing season (1 August 2016) in the fenced pasture, followed by the mowed pasture and the grazing pasture, and the opposite trend was observed at the end of the growing season (30 September 2016). From the difference maps (Figure 4 (c) and (f)), low percentage differences ((Landsat LAI-Sentinel-2A LAI)× 100/Sentinel-2A LAI) close to zero were observed in the low-LAI areas (grazing pasture on 1 August and mowed pasture on 30 September) and in the high LAI areas (mowed pasture on 1 August and grazing pasture on 30 September). However, a difference was still observed between the

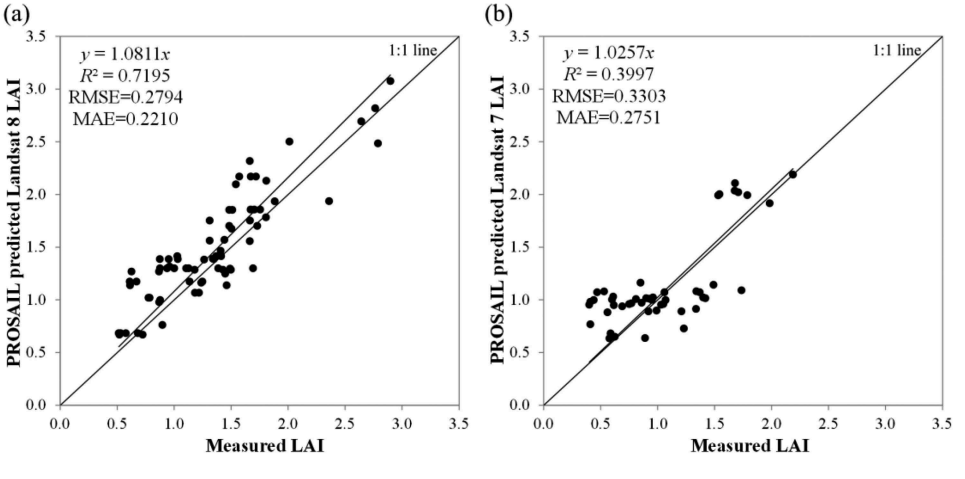

Figure 3. Scatter plot of ground-measured LAI and PROSAIL-predicted LAI based on Landsat 8 (a) and Landsat 7 (b) images.

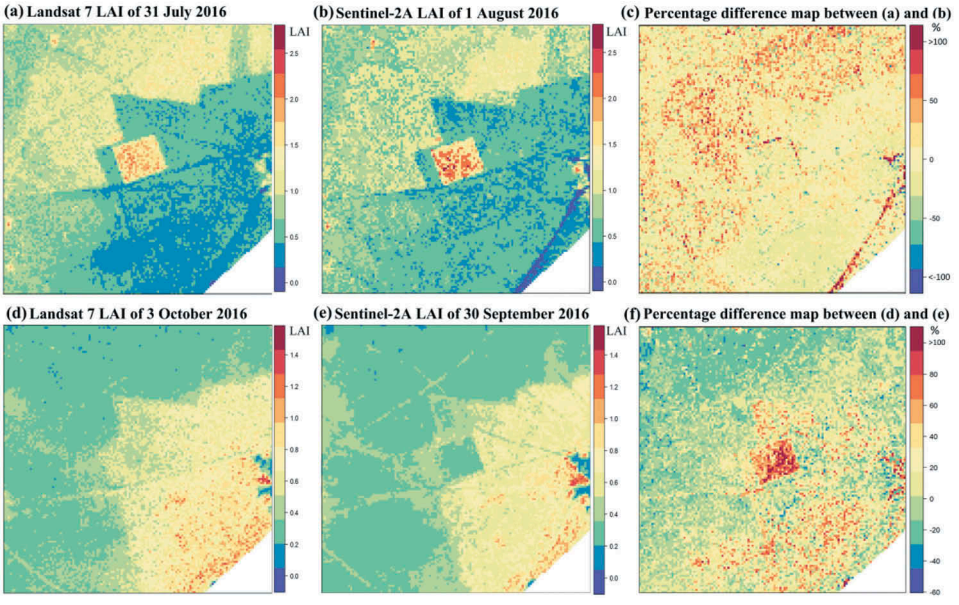

Figure 4. PROSAIL-generated LAI maps from Landsat 7 ((a) and (d)) and Sentinel-2A ((b) and (e)) and their percentage difference maps ((difference/Sentinel-2A LAI)× 100, (c) and (f)). The Landsat 7 and Sentinel-2A images used in the top row were acquired on 31 July 2016 and 1 August 2016, and those in the bottom row were acquired on 3 October 2016 and 30 September 2016, respectively.

Landsat LAI maps and Sentinel LAI maps, especially in the fenced pasture. The difference may have been caused by the different spatial and spectral characteristics (number of bands, bandwidth and spatial resolution) of the three satellite sensors used in the PROSAIL model (Table 2). Only five bands of the Landsat images with a 30-m spatial resolution were used, whereas nine bands of Sentinel-2A images with a 20-m spatial resolution were input into the PROSAIL LUT. In the fenced pasture, large amounts of litter and withered leaves had accumulated, which can influence the correct detection of the green part of the grassland canopy. In the middle of the growing season (1 August 2016), the greater spatial resolution of the Landsat images (30 m) indicated that non-green information was detected, and lower LAI values in the fenced pasture were predicted for the Landsat LAI maps. At the end of the growing season (30 September 2016), the greater spatial resolution of the Landsat images (30 m) indicated that more green information was detected, so higher LAI values in the fenced pasture and grazing pasture were predicted for the Landsat LAI maps. Moreover, the Sentinel-2A SR images used in this study include three more vegetation red edge bands (bands 5, 6, and 7) and one more SWIR band (band 11) than the Landsat images. These bands are more sensitive to background information (litter and soil), which can also result in a difference between the Landsat LAI maps and Sentinel LAI maps. Scatter plots of the LAI maps retrieved from the two sets of satellite imagery on the two overpass days are shown in Figure 5. Good agreement was observed for the two pairs of LAI maps. The R^2 and RMSE values were 0.64 and 0.24, respectively, for this pair on 1 August 2016 and 0.78 and 0.13, respectively, for the pair on 30 September 2016. Most of the pixels of the LAI difference maps are between ± 0.5 on 1 August and ± 0.3 on 30 September.

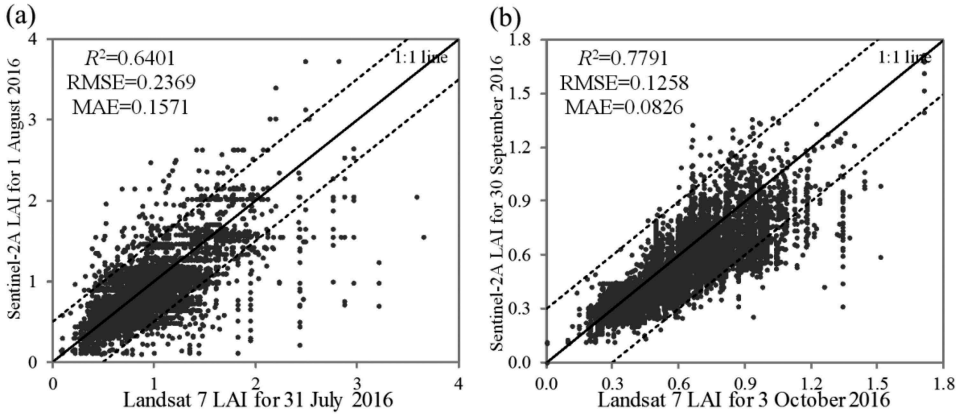

Figure 5. Scatter plots of the Landsat and Sentinel-2A retrieved LAI.

4.1.3 *Assessing PROSAIL-generated MODIS LAI maps*

To assess the PROSAIL-generated MODIS LAI maps, the ground-measured LAI values on the experiment dates in the mowed pasture and grazing pasture were averaged and were considered to be the 'true' values. The upscaled 500 m Landsat and Sentinel-2A LAI, MCD43A4_PROSPECT LAI and gap-filled 4-day MCD15A3H LAI map pixels that contained ground measurements were also averaged and were then compared to the ground measurements. The temporal variations in these products are shown in Figure 6.

Figure 6 shows that the gap-filled MCD15A3H LAI product has higher LAI values than the MCD43A4_PROSPECT LAI product in both the mowed pasture and the grazing pasture, and the higher LAI values are more evident in the grazing pasture. Compared to the ground-measured LAI and upscaled finer-resolution LAI maps, the gap-filled MCD15A3H LAI and MCD43A4_PROSPECT LAIs all exhibited reasonable estimations in the mowed pasture. The two datasets had seasonal variations similar to that observed in the reference LAI, and the gap-filled MCD15A3H LAI performed slightly better than the MCD43A4_PROSPECT LAI. In the grazing pasture, however, a clear overestimation was observed for the gap-filled MCD15A3H LAI. This gap was also observed in our previous study on MOD15 and MCD15 LAI products for this site. The reason for the gap may lie in the sparse grass and bare soil; the red and NIR reflectance bands that are used in the MCD15 LAI products algorithm cannot effectively eliminate the influence of the soil background on the LAI modeling (Li et al. 2014, 2015). In comparison, our estimated MCD43A4_PROSPECT LAI was closer to the measured LAI and Landsat LAI except during the growing season in 2014, when the MCD43A4_PROSPECT LAI was higher than the reference LAI. This result may have been caused by insufficient ground measurements in the grazing pasture DURING this period; the average value in this pasture cannot represent that of the MODIS LAI pixels. In addition, the low vegetation coverage during the peak growing season in the grazing pasture and the large pixel size of the MODIS product (500 m) can lead to higher LAI values of the MODIS LAI product because of the scale effect. The estimated MCD43A4_PROSPECT LAI DATA also exhibit a smoother seasonal trajectory and had fewer anomalous points than the gap-filled MCD15A3H LAI data. A check of the QC layer of the MCD15A3H LAI product indicated that the anomalous points were mainly caused by the failure of the gap filling method (fail gap-filled MCD15A3H LAI

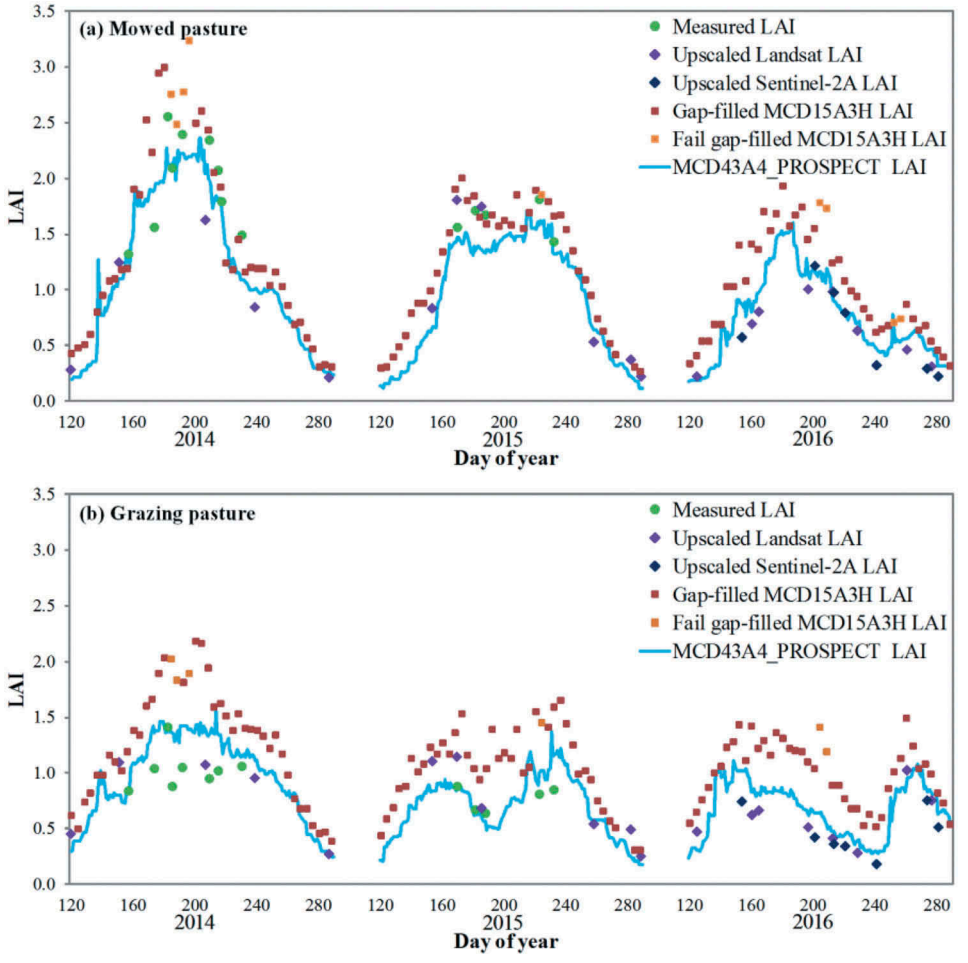

Figure 6. Temporal variabilities of the PROSAIL-generated MCD43A4_PROSPECT LAI compared with the gap-filled MCD15A3H LAI, upscaled Landsat LAI, upscaled Sentinel-2A LAI, and measured LAI in the mowed pasture (a) and grazing pasture (b).

points in Figure 6). Another reason for the smooth MCD43A4_PROSPECT LAI curve may be that even though MCD43A4 is a daily product, it is produced from a 16-day period using data smoothing and may miss some abrupt changes.

4.2 *STARFM performance*

4.2.1 *Comparison to ground measurements*

The results from the two daily 30 m LAI datasets generated from the two strategies were validated using the remaining 221 ground measurements that were not collected on the Landsat overpass dates. The STARFM-predicted 30 m daily LAI maps based on the MCD15A3H-Landsat (Sentinel) LAI pairs (MCD15A3H_STARFM LAI) and the MCD43A4-Landsat (Sentinel) LAI pairs (MCD43A4_PROSPECT_STARFM LAI) were validated, and scatter plots of the measured and predicted LAI vales based on the two datasets are shown in

Figure 7. The MCD43A4_PROSPECT_STARFM LAI is more similar to the ground-measured LAI than the MCD15A3H_STARFM LAI, and the data points in the scatter plot are closer to the 1:1 line (R^2 = 0.65 compared to 0.55 for the MCD15A3H_STARFM LAI). The RMSE and MAE between the ground-measured LAI and MCD43A4_PROSPECT_STARFM LAI are 0.44 and 0.34, respectively, which represents an improvement over the MCD15A3H_STARFM LAI (RMSE = 0.56 and MAE = 0.42).

Considering the different pasture types in the study site, the MCD15A3H_STARFM LAI and MCD43A4_PROSPECT_STARFM LAI both have a good performance in the grazing pasture and the mowed pasture (Table 4). The bias between the predicted LAI and measured LAI is less than 0.2. The MCD43A4_PROSPECT_STARFM LAI performed slightly better than the MCD15A3H_STARFM LAI and had smaller RMSE, MAE, and bias values. For the fenced pasture, a larger variation in the two predicted LAI datasets from the ground LAI was observed; the MCD15A3H_STARFM LAI and MCD43A4_PROSPECT_STARFM LAI both underestimated the ground LAI with a negative bias. The reason for this result is the small area of the fenced pasture (650 m × 550 m), which appeared as mixed pixels that were combined with the neighboring pastures on the 500 m MODIS product. STARFM can reasonably preserve the high spatial resolution of Landsat imagery and the high temporal resolution of MODIS imagery if pure coarse-resolution neighboring pixels can be found within the moving window (Gao et al. 2015). Because mixed pixels consist of several land use types that have different seasonal variations, the performance will decrease somewhat if 'pure' pixels cannot be found with the moving window (Gao, Schwaller, and Hall 2006).

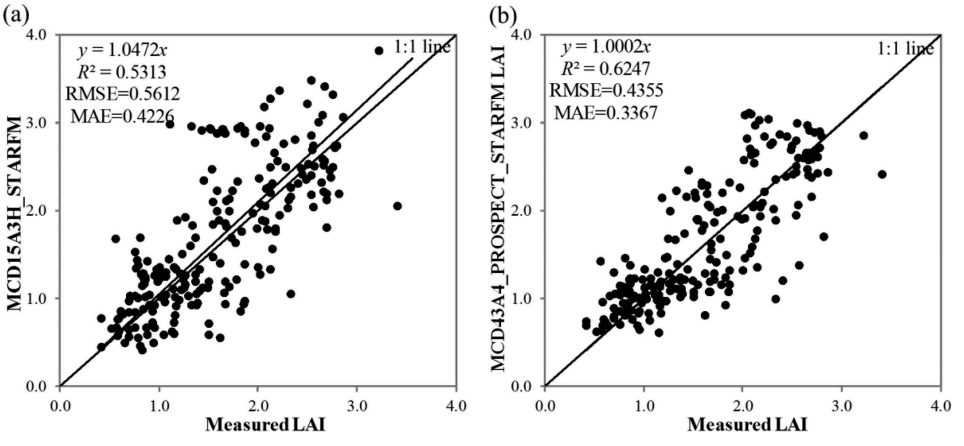

Figure 7. Validation of the MCD15A3H_STARFM LAI (a) and MCD43A4_PROSPECT_STARFM LAI (b) using the ground-measured LAI.

Table 4. Statistical differences between the STARFM-fused daily LAI and the ground-measured LAI.

		MCD43A4_PROSPECT_STARFM LAI			MCD15A3H_STARFM LAI		
Pasture type	Number	RMSE	MAE	Bias	RMSE	MAE	Bias
Grazing pasture	86	0.35	0.26	0.08	0.43	0.34	0.04
Mowed pasture	131	0.47	0.37	0.05	0.62	0.46	0.20
Fenced pasture	4	0.80	0.74	−0.74	0.84	0.76	−0.01

4.2.2 *Comparison to Landsat/Sentinel-2A images*

The predicted Landsat-like LAI maps were also compared with actual Landsat/Sentinel-2A LAI maps (Figure 8). The two pairs of Landsat and MODIS LAI maps were acquired from 31 July and 3 October 2016 (observation dates), and two additional MODIS LAI maps were acquired on 1 August and 30 September 2016 (prediction dates). The STARFM algorithm was used to predict LAI maps on 1 August and 30 September using a data pair on the closest observation date and the MODIS LAI map from the prediction date. The predicted LAI maps were then compared with the actual Landsat or Sentinel LAI maps. The predicted Landsat-like LAI maps are visually similar to the actual images, especially for 31 July and 3 October, which use the same predicted MODIS LAI maps as those in the Landsat-MODIS pairs. The predicted LAI maps perfectly reconstructed the LAI maps. The predicted LAI maps on 1 August and 30 September consistently reconstructed the spatial patterns of the Landsat LAI maps that compose the Landsat-MODIS pairs, and the reconstructions were also visually similar to the actual LAI maps. Figure 9 compares the scatter plots of the predicted Landsat-like LAI maps with those of the actual Landsat/Sentinel-2A LAI maps. The data points plot close to the 1:1 line in each panel, indicating that the predictions were in good agreement with the actual LAI maps. The R^2 values of the predicted LAI maps on 31 July and 3 October against the actual LAI maps are higher than 0.99, and the RMSE and MAE values are lower than 0.005 and 0.005, respectively. For the predicted LAI maps for 1 August and 30 September, even though a difference was observed between the predicted LAI maps and the actual Sentinel LAI maps, which may have been caused by the different satellite images used to predict (Landsat7 LAI) and validate (Sentinel-2A LAI) the LAI maps, the R^2

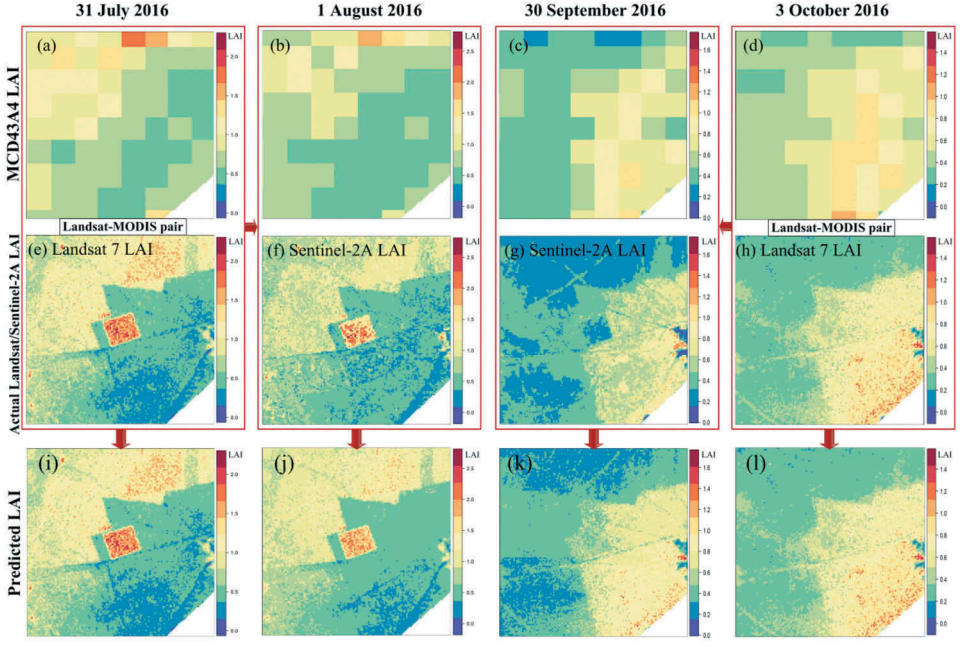

Figure 8. Illustration of STARFM-predicted 30m LAI maps ((i), (j), (k) and (l)) and comparisons with actual Landsat/Sentinel-2 LAI maps ((e), (f), (g) and (h)).

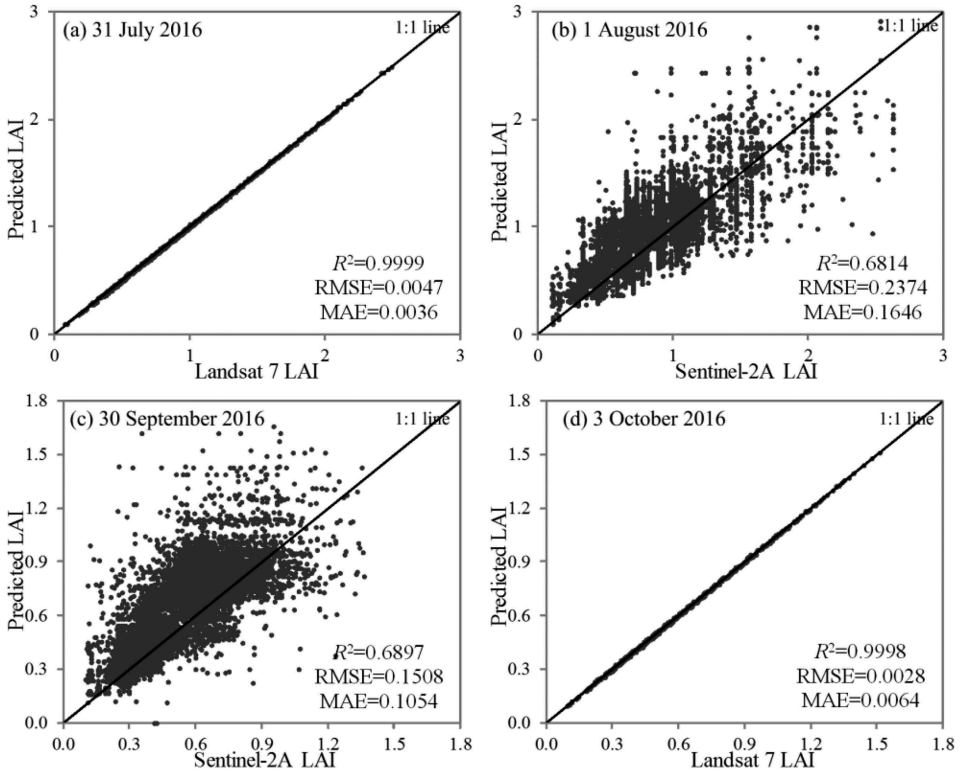

Figure 9. Scatter plots of actual Landsat/Sentinel-2 LAIs and predicted Landsat-like LAIs.

values of the predicted images against the actual images were still higher than 0.68, and the RMSE and MAE values were 0.24 and 0.16 for 1 August and 0.15 and 0.11 for 30 September, respectively.

4.2.3 *Temporal comparison*

To further investigate the performance of STARFM, time series of the fused daily MCD15A3H_STARFM LAI and fused daily MCD43A4_PROSPECT_STARFM LAI were compared to the daily MCD43A4_PROSPECT LAI, Landsat (Sentinel-2A)-derived LAI and ground-measured LAI for the three pasture types (Figure 10). After fusing the data using STARFM, the accuracies of the MCD15A3H_STARFM LAI and MCD43A4_PROSPECT_STARFM LAI were further improved compared to the MCD43A4_PROSPECT LAI and MCD15A3H LAI, and the two datasets were more similar to the ground measurements and were more consistent with the Landsat (Sentinel-2A)-derived LAI in the mowed pasture and grazing pasture. However, an obvious fluctuation was observed in the grazing pasture around DOY 177 in 2014, which was caused by the long interval between the available Landsat/Sentinel acquisitions in the middle of the growing season. The available fine-resolution images with the closest date were the Sentinel-2A images acquired on DOYs 154 and 201; the Sentinel-MODIS data pair acquired on DOY 154 was used to predict the LAI maps between DOYs 153 and 177, and the Sentinel-MODIS data pair acquired on DOY 201 was used to predict the LAI maps between DOYs 178 and 204. Because of the grazing activity, the vegetation cover in

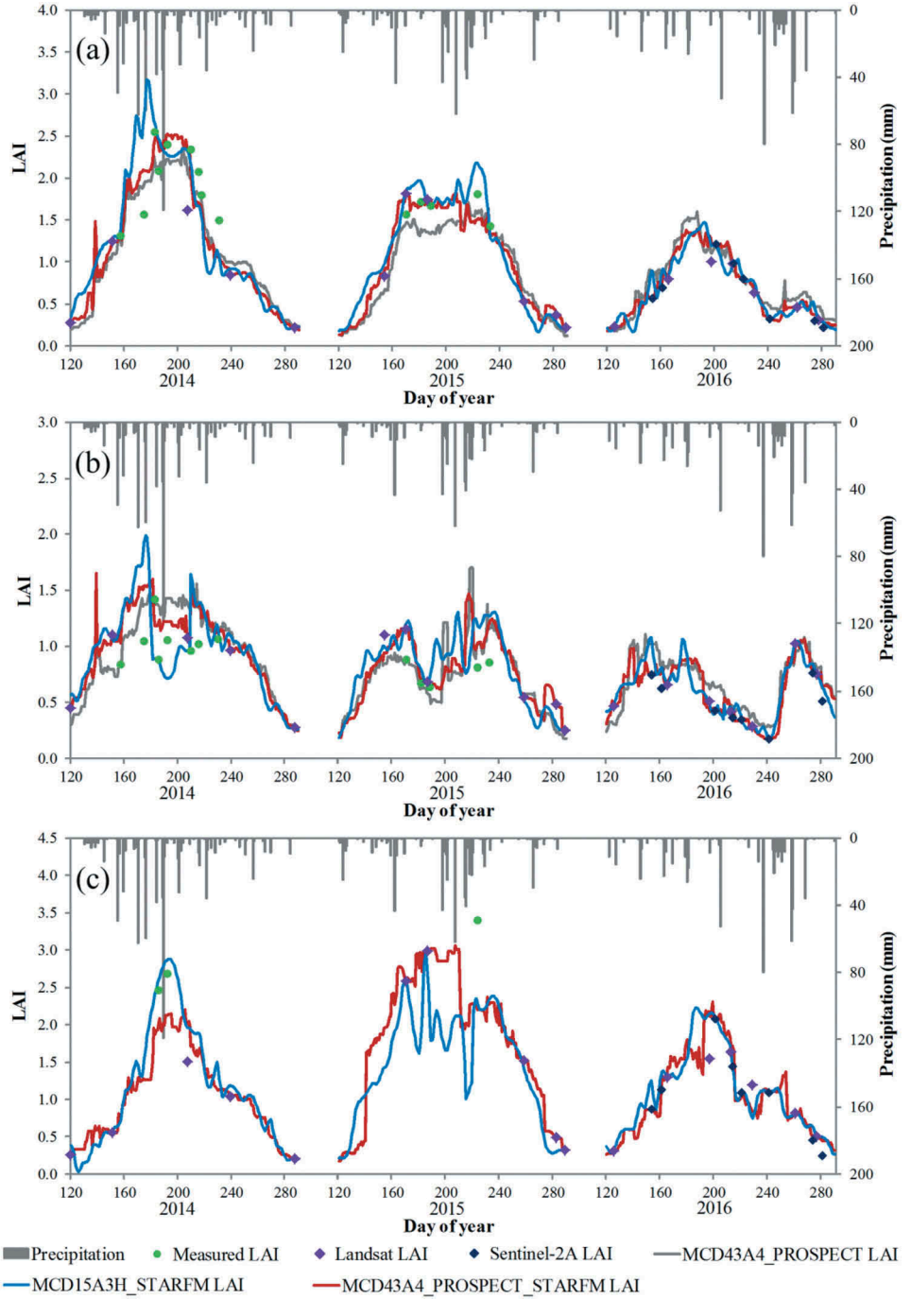

Figure 10. Temporal variabilities of the MCD43A4_PROSPECT_STARFM LAI and MCD15A3H_STARFM LAI with the MCD43A4_PROSPECT LAI, Landsat LAI, Sentinel-2A LAI, and measured LAI in the mowed pasture (a), grazing pasture (b) and fenced pasture (c).

the grazing pasture was lower on DOY 201 than on DOY 154, and the MODIS LAI products significantly overestimated the ground-measured LAI and Sentinel LAI on DOY 201 and slightly underestimated the Sentinel LAI on DOY 154 (Figure 10). The different performances of the two Sentinel-MODIS data pairs resulted in fluctuations in the predicted LAI maps of the grazing pasture on DOY 177 in 2014. Because of the smaller patch size, the fenced pasture appeared as mixed pixels that were combined with the neighboring pastures on the 500-m MODIS product. The mixed pixels also have lower LAI values than the pixels of the fenced pasture due to the lower LAIs in the mowed pasture and grazing pasture; spectrally similar 'pure' pixels cannot be found within the moving window in the study area, so the ground LAI is still underestimated in the fused MCD43A4_PROSPECT_STARFM LAI product. However, the MCD15A3H_STARFM LAI had a comparable curve to the ground measurements and higher values than the MCD43A4_PROSPECT_STARFM LAI in the early steady period of the growing season of 2014 in the fenced pasture. These values were produced from highly anomalous points using the spline interpolation method. For the fused daily MCD15A3H_STARFM LAI, which was interpolated from fused four-day MCD15A3H_STARFM LAI data using a cubic spline interpolation method, daily fluctuations are notable, particularly during the peak period of the growing season, when clouds were more frequent. The MCD43A4_PROSPECT_STARFM LAI had a smoother seasonal trajectory.

5 Discussion

5.1 *LAI variability in different pasture types*

The LAI values in the three pasture types had different seasonal dynamics and interannual variations, which have rarely been considered in previous large-scale grassland research. In the mowed pasture, grass grows naturally until the middle of the peak period at the end of July or early August, when the LAI reaches its highest value. The hay-cutting activities result in an early decrease of the LAI. In the grazing pasture, animals start grazing in early June, which stops the increase in LAI and can even cause a rapid decrease in LAI. The temporal trajectory of the LAI value in the fenced pasture represents the natural growth of grass. Because of the small patch of fenced pasture in our study (smaller than one MODIS pixel, and there are no spectrally similar pure MODIS-sized pixels in the study area), the STARFM failed to capture its temporal variation (Gao et al. 2015; Gao, Schwaller, and Hall 2006). In Inner Mongolia, China, our previous study found that 10.65% of the total grassland area was used as mowed pasture (Tang et al. 2015a; Tang et al. 2015b). For forage storage and precise management at the pasture scale, our dense time scale LAI is useful for providing time-critical information about the within-field variability for optimizing family pasture management.

The impact of climate conditions on the LAI variability in different pasture types was also analyzed. Precipitation was found to be significantly correlated with the LAI variability (Figure 10), but the temperature had little influence on changes in LAI (not shown in this paper). More precipitation fell in 2014 (405.9 mm) than in 2015 (289.9 mm) and 2016 (349.0 mm), especially during the periods in which the LAI increased; thus, higher LAI values were observed during the stable LAI period in the mowed pasture and grazing pasture in 2014. The fenced pasture was expected to have the same trend; however, a fire occurred in the pasture before the growing season (late April) in this

pasture, and all of the dead vegetation that had accumulated over the previous ten years was removed, which resulted in faster grass growth and a higher LAI value during the stable LAI period in 2015. Fast grass growth also occurred in 2016, but it was slower than in 2015 because most of the grass had recovered (West and Hassan 1985). In 2015, several heavy rainfall events occurred during the late stable LAI period, which delayed the period of decreasing LAI and resulted in a longer stable LAI period. The periods in 2016 during which the LAI increased and remained constant had little rainfall, which resulted in a lower LAI values during the constant LAI period, an earlier decrease of LAI and a shorter period of constant LAI values. However, several heavy rainfall events occurred at the end of the growing season in 2016 and resulted in grass regrowth.

5.2 *MODIS LAI product performance*

Our previous results showed a slight overestimation and a clear seasonal anomaly of the 8-day MODIS Collection 5 LAI products (MOD15 and MCD15) compared to the ground measurements and high resolution LAI maps in the grassland area (Li et al. 2014, 2015), which were mainly the resulted of surface reflectance uncertainty after checking the quality control layers (Li et al. 2015). In this study, the 4-day MCD15A3H LAI product (version 6) showed high accuracy and a smooth seasonal trajectory; the better performance may be attributed to the higher spatial resolution (500 m), the shorter composite data (4 days) and the improved surface reflectance input. A higher spatial resolution can decrease the number of mixed pixels and improve the definition of the biome type classification for each pixel to reduce the heterogeneity in coarse pixels (Yan et al. 2016a). Moreover, a new MODIS daily surface reflectance that employed an improved aerosol retrieval and correction algorithm and a new version of the MODIS land-cover product were also used to generate the MCD15A3H LAI product (Yan et al. 2016a).

5.3 *Advantages and limitations of the method*

In this study, fused high-spatial resolution Landsat and Sentinel-2A LAI maps and high temporal resolution MODIS LAI maps were generated using a one-dimensional canopy radiative transfer model (PROSAIL). The results demonstrated good performance compared to the ground measurements and the MCD15A3H LAI product. Even though MODIS LAI products adopt a more sophisticated 3-D radiative transfer approach (Knyazikhin et al. 1998), the 3-D model exhibits increased complexity and requires more complicated parameterization, but there was no clear evidence that these measures increased the model accuracy (Pasolli et al. 2015; Pinty et al. 2001). In comparison, by calibrating the PROSAIL radiative transfer model to the specific characteristics of the study area using background information, the ill-posed problems associated with the inversion process were limited, and the model was better able to match the range of target values (Combal et al. 2003). Thus, the model and inversion strategy have been successfully applied in many studies to retrieve the LAI from multi-temporal and multi-resolution images (Pasolli et al. 2015; Campos-Taberner et al. 2017, 2016; Si et al. 2012).

STARFM was originally designed to generate daily surface reflectance at the Landsat scale by fusing temporally sparse Landsat imagery with daily collected MODIS imagery. The model was successfully used in this study to fuse LAI products generated from the PROSAIL

model. By searching for spectrally similar pixels within the moving window, the predicted high-spatio-temporal resolution images can both capture temporal variations in MODIS time series and preserve the high-resolution spatial details in Landsat images. For small patches with high numbers of values (e.g., the fenced pasture in this study) for which a pure MODIS-sized pixel cannot be found in the search window, the prediction will most likely have larger prediction errors (Gao et al. 2015; Gao, Schwaller, and Hall 2006). Further studies may use the near-daily project for on-board autonomy-vegetation (PROBA-V) dataset produced by the European Space Agency, which has a spatial resolution as high as 100 m (Francois et al. 2014). The daily visible infrared imaging radiometer suite (VIIRS) on board the suomi national polar-orbiting partnership (NPP) platform with a 37 m spatial resolution (Cao et al. 2013) offers a higher spatial resolution, which may help identify more pure coarse-resolution neighboring pixels and decrease the prediction error for landscapes with small patches. Another requirement for good STARFM performance is an even seasonal distribution of clear Landsat-scale images (Gao et al. 2017). In cloudy areas, using only Landsat images is insufficient, and other sources of high-spatial resolution images are required to provide more temporal information about canopy changes that occur between Landsat overpass dates. In this study, the Sentinel-2A data, which combines a high spatial resolution, wide field of view and spectral coverage, were combined with Landsat data to increase the high-spatial resolution observation frequency. Sentinel-2B was launched in 2017 and can provide more frequent fine-resolution observations.

This study used a simple gap filling method to fill in the LAI values of cloudy pixels with the aim of avoiding changing high-quality LAI values that were identified by the product QC layer. The fused 4-day MCD15A3H_STARFM LAI data were then interpolated to daily time steps using a cubic spline interpolation method. Even through the simple gap filling method can eliminate most of the anomalous points from the original LAI curves, the remaining anomalous fluctuation in the LAI time series will still result in large uncertainties in the spline interpolation and in unsmoothed daily LAI curves. Thus, future studies may adopt more advanced time series data algorithms such as the Savitzky-Golay (SG) filter (Savitzky and Golay 1964; Gao et al. 2008) and the harmonic analysis of NDVI time series (HANTS) algorithm (Roerink, Menenti, and Verhoef 2000), to replace missing or poor-quality observations and produce temporally smoothed and spatially complete data sets.

6 Conclusions

An LAI-retrieving framework was developed in this study to achieve both high-spatial (30 m) and temporal (daily) resolution LAI datasets over a meadow steppe site in northern China. The PROSAIL model was applied to gap-filled Landsat, Sentinel-2A and MODIS surface reflectance images to generate LAI maps, and daily 30 m LAI data were predicted using the STARFM algorithm, which can preserve the high spatial resolution of Landsat images and the high temporal resolution of MODIS data. The results were assessed for three types of pastures (mowed pasture, grazing pasture, and fenced pasture) using ground measurements from 2014–2015. The results demonstrated the good performance of the PROSAIL model in retrieving LAI from Landsat, Sentinel-2A and MODIS images: the RMSE of the Landsat 7 and Landsat 8 LAI against the observed LAI were 0.33 and 0.28 respectively. The MCD43A4-derived LAI also had higher accuracy than the MCD15A3H LAI with fewer anomalous points and a seasonal variation that was

closer to those of the observations and the Landsat LAI. Due to the lack of ground-measured LAI in 2016, the PROSAIL-generated Sentinel-2A and Landsat LAI maps were compared and showed good agreement and similar spatial patterns with LAI differences between ± 0.5. The use of Sentinel-2A data has effectively increased landscape vegetation observation frequencies and provides temporal information about canopy changes occurring between Landsat overpass dates. Evaluations using ground measurements indicate that STARFM-fused daily LAI estimates using Sentinel-2A, Landsat and MCD43A4_PROSPECT LAI inputs have high accuracy, with an RMSE of 0.44 and an MAE of 0.34, which is an improvement over fused MCD15A3H_STARFM LAI data, which have an RMSE of 0.56 and an MAE of 0.42 with the ground measurements. The MCD43A4_PROSPECT_STARFM LAI is more similar to the ground measurements, is more consistent with the Landsat (Sentinel-2A)-derived LAI than the MCD43A4_PROSPECT LAI data and exhibited a smoother seasonal trajectory than the MCD15A3H_STARFM LAI data. The LAI data fusion results captured the different temporal variations of the three pasture types. The interannual difference within one pasture is mainly controlled by the precipitation. The LAI data fusion results are better for the grazing and mowed pastures. However, for the fenced pasture, which has small patch sizes and high LAI values, the performance of STARFM is degraded. Finally, although the area of the study site is limited (only 4 km× 4 km), the biomes studied are representative of meadow steppes in northern China. The scheme developed in this study can serve as a reference for future studies of larger regions and can be applied to additional types of grasslands.

Acknowledgments

This work was supported by the National Key Research and Development Program of China (2016YFC0500608; 2017YFE0104500), the National Natural Science Foundation of China (41471093), China Agriculture Research System (CARS–34), Public Sector Projects in the Ministry of Agriculture (201303060), Fundamental Research Funds for Central Non-profit Scientific Institution (No.1610132016033; No.1610132016027), and National High-tech Research and Development Projects(863) (2012AA102003-4). We would also like to thank for the scholarship support from the China Scholarship Council. We acknowledge the NASA Land Processes Distributed Active Archive Center (LP DAAC), USGS/Earth Resources Observation and Science (EROS) Center for providing Landsat 7, Landsat 8, Sentinel-2A, and MODIS data.

Disclosure statement

No potential conflict of interest was reported by the authors.

Funding

This work was supported by the national Key R&D Program of China [2016YFC0500608, 2017YFE0104500]; National Natural Science Foundation of China [41471093]; National High-tech R&D Program of China (863 Program) [2012AA102003-4]; China Agriculture Research System [CARS–34]; Public Sector Projects in the Ministry of Agriculture [201303060] and Fundamental Research Funds for Central Non-profit Scientific Institution [No.1610132016033; No.1610132016027];

ORCID

Zhenwang Li http://orcid.org/0000-0002-9882-8986
Chengquan Huang http://orcid.org/0000-0003-0055-9798
Zhiliang Zhu http://orcid.org/0000-0002-6860-6936

References

Allen, W. A., H. W. Gausman, A. J. Richardson, and J. R. Thomas. 1969. "Interaction of Isotropic Light with a Compact Plant Leaf*." *Journal of the Optical Society of America* 59 (10): 1376–1379. doi:10.1364/josa.59.001376.

Anderson, M. C., W. P. Kustas, J. M. Norman, C. R. Hain, J. R. Mecikalski, L. Schultz, M. P. González-Dugo et al. 2011. "Mapping Daily Evapotranspiration at Field to Continental Scales Using Geostationary and Polar Orbiting Satellite Imagery." *Hydrology and Earth System Sciences* 15 (1): 223. DOI:10.5194/hess-15-223-2011.

Arvidson, T., S. Goward, J. Gasch, and D. Williams. 2006. "Landsat-7 Long-Term Acquisition Plan." *Photogrammetric Engineering & Remote Sensing* 72 (10): 1137–1146. doi:10.14358/pers.72.10.1137.

Asner, G. P., J. M. O. Scurlock, and J. A. Hicke. 2003. "Global Synthesis of Leaf Area Index Observations: Implications for Ecological and Remote Sensing Studies." *Global Ecology and Biogeography* 12 (3): 191–205. doi:10.1046/j.1466-822X.2003.00026.x.

Baret, F., M. Weiss, R. Lacaze, F. Camacho, H. Makhmara, P. Pacholcyzk, and B. Smets. 2013. "GEOV1: LAI and FAPAR Essential Climate Variables and FCOVER Global Time Series Capitalizing over Existing Products. Part1: Principles of Development and Production." *Remote Sensing of Environment* 137: 299–309. doi:10.1016/j.rse.2012.12.027.

Baret, F., and S. Buis. 2008. "Estimating Canopy Characteristics from Remote Sensing Observations. Review of Methods and Associated Problems." In *Advances in Land Remote Sensing: System, Modeling, Inversion and Application*, edited by S. Liang, 173–201. Dordrecht: Springer. doi:10.1007/978-1-4020-6450-0_7

Baret, F., O. Hagolle, B. Geiger, P. Bicheron, B. Miras, M. Huc, B. Berthelot, et al. 2007. "LAI, fAPAR and fCover CYCLOPES Global Products Derived from VEGETATION." *Remote Sensing of Environment* 110 (3): 275–286. doi:10.1016/j.rse.2007.02.018.

Bonan, G. B. 1993. "Importance of Leaf Area Index and Forest Type When Estimating Photosynthesis in Boreal Forests." *Remote Sensing of Environment* 43 (3): 303–314. doi:http://dx.doi.org/10.1016/0034-4257(93)90072-6.

Campos-Taberner, M., F. García-Haro, G. Camps-Valls, G. Grau-Muedra, F. Nutini, L. Busetto, D. Katsantonis et al. 2017. "Exploitation of SAR and Optical Sentinel Data to Detect Rice Crop and Estimate Seasonal Dynamics of Leaf Area Index." *Remote Sensing* 9 (3): 248. DOI:10.3390/rs9030248.

Campos-Taberner, M., J. A. García-Haro, G. Camps-Valls, G. Grau-Muedra, F. Nutini, A. Crema, and M. Boschetti. 2016. "Multitemporal and Multiresolution Leaf Area Index Retrieval for Operational Local Rice Crop Monitoring." *Remote Sensing of Environment* 187: 102–118. doi:10.1016/j.rse.2016.10.009.

Cao, C., J. Xiong, S. Blonski, Q. Liu, S. Uprety, X. Shao, Y. Bai, and F. Weng. 2013. "Suomi NPP VIIRS Sensor Data Record Verification, Validation, and Long-Term Performance Monitoring."." *Journal of Geophysical Research: Atmospheres 118*, no. 20: 11,664–11,78. doi:10.1002/2013jd020418.

Chen, J. M., and T. A. Black. 1992. "Defining Leaf Area Index for Non-Flat Leaves." *Plant, Cell & Environment* 15 (4): 421–429. doi:10.1111/j.1365-3040.1992.tb00992.x.

Colombo, R., D. Bellingeri, D. Fasolini, and C. M. Marino. 2003. "Retrieval of Leaf Area Index in Different Vegetation Types Using High Resolution Satellite Data." *Remote Sensing of Environment* 86 (1): 120–131. doi:10.1016/S0034-4257(03)00094-4.

Combal, B., F. Baret, M. Weiss, A. Trubuil, D. Mace, A. Pragnere, R. Myneni, Y. Knyazikhin, and L. Wang. 2003. "Retrieval of Canopy Biophysical Variables from Bidirectional Reflectance: Using

Prior Information to Solve the Ill-Posed Inverse Problem." *Remote Sensing of Environment* 84 (1): 1–15. doi:10.1016/S0034-4257(02)00035-4.

Coops, N. C., M. A. W. Matt Johnson, and J. C. White. 2006. "Assessment of QuickBird High Spatial Resolution Imagery to Detect Red Attack Damage Due to Mountain Pine Beetle Infestation." *Remote Sensing of Environment* 103 (1): 67–80. doi:10.1016/j.rse.2006.03.012.

Darvishzadeh, R., A. Skidmore, M. Schlerf, and C. Atzberger. 2008. "Inversion of a Radiative Transfer Model for Estimating Vegetation LAI and Chlorophyll in a Heterogeneous Grassland." *Remote Sensing of Environment* 112 (5): 2592–2604. doi:10.1016/j.rse.2007.12.003.

De Kauwe, M. G., M. I. Disney, T. Quaife, P. Lewis, and M. Williams. 2011. "An Assessment of the MODIS Collection 5 Leaf Area Index Product for a Region of Mixed Coniferous Forest." *Remote Sensing of Environment* 115 (2): 767–780. doi:10.1016/j.rse.2010.11.004.

Dorigo, W. A., R. Zurita-Milla, A. J. W. De Wit, J. Brazile, R. Singh, and M. E. Schaepman. 2007. "A Review on Reflective Remote Sensing and Data Assimilation Techniques for Enhanced Agroecosystem Modeling." *International Journal of Applied Earth Observation and Geoinformation* 9 (2): 165–193.

Drusch, M., U. Del Bello, S. Carlier, O. Colin, V. Fernandez, F. Gascon, B. Hoersch, et al. 2012. "Sentinel-2: ESA's Optical High-Resolution Mission for GMES Operational Services." *Remote Sensing of Environment* 120 :25–36. doi:10.1016/j.rse.2011.11.026.

Feret, J.-B., C. François, G. P. Asner, A. A. Gitelson, R. E. Martin, L. P. R. Bidel, S. L. Ustin, G. Le Maire, and S. Jacquemoud. 2008. "PROSPECT-4 and 5: Advances in the Leaf Optical Properties Model Separating Photosynthetic Pigments." *Remote Sensing of Environment* 112 (6): 3030–3043. doi:10.1016/j.rse.2008.02.012.

Frampton, W. J., J. Dash, G. Watmough, and E. J. Milton. 2013. "Evaluating the Capabilities of Sentinel-2 for Quantitative Estimation of Biophysical Variables in Vegetation." *ISPRS Journal of Photogrammetry and Remote Sensing* 82: 83–92. doi:10.1016/j.isprsjprs.2013.04.007.

Francois, M., S. Santandrea, K. Mellab, D. Vrancken, and J. Versluys. 2014. "The PROBA-V Mission: The Space Segment." *International Journal of Remote Sensing* 35 (7): 2548–2564. doi:10.1080/01431161.2014.883098.

Ganguly, S., R. R. Nemani, G. Zhang, H. Hashimoto, C. Milesi, A. Michaelis, W. Wang, et al. 2012. ""Generating Global Leaf Area Index from Landsat." *Algorithm Formulation and Demonstration.*" *Remote Sensing of Environment* 122 :185–202. doi:10.1016/j.rse.2011.10.032.

Gao, F., T. Hilker, X. Zhu, M. Anderson, J. Masek, P. Wang, and Y. Yang. 2015. "Fusing Landsat and MODIS Data for Vegetation Monitoring." *IEEE Geoscience and Remote Sensing Magazine* 3 (3): 47–60. doi:10.1109/mgrs.2015.2434351.

Gao, F., J. T. Morisette, R. E. Wolfe, G. Ederer, J. Pedelty, E. Masuoka, R. Myneni, B. Tan, and J. Nightingale. 2008. "An Algorithm to Produce Temporally and Spatially Continuous MODIS-LAI Time Series." *IEEE Geoscience and Remote Sensing Letters* 5 (1): 60–64. doi:10.1109/lgrs.2007.907971.

Gao, F., M. C. Anderson, W. P. Kustas, and Y. Wang. 2012. "Simple Method for Retrieving Leaf Area Index from Landsat Using MODIS Leaf Area Index Products as Reference." *Journal of Applied Remote Sensing* 6 (1): 1–15.

Gao, F., M. C. Anderson, X. Zhang, J. G. Zhengwei Yang, W. P. Alfieri, R. M. Kustas, D. M. Johnson, and J. H. Prueger. 2017. "Toward Mapping Crop Progress at Field Scales through Fusion of Landsat and MODIS Imagery." *Remote Sensing of Environment* 188: 9–25. doi:10.1016/j.rse.2016.11.004.

Gao, F. J., M. M. Schwaller, and F. Hall. 2006. "On the Blending of the Landsat and MODIS Surface Reflectance: Predicting Daily Landsat Surface Reflectance." *IEEE Transactions on Geoscience and Remote Sensing* 44 (8): 2207–2218. doi:10.1109/tgrs.2006.872081.

Gastellu-Etchegorry, J. P., F. Gascon, and P. Estève. 2003. "An Interpolation Procedure for Generalizing a Look-Up Table Inversion Method." *Remote Sensing of Environment* 87 (1): 55–71. doi:10.1016/S0034-4257(03)00146-9.

Goel, N. S. 1988. "Models of Vegetation Canopy Reflectance and Their Use in Estimation of Biophysical Parameters from Reflectance Data." *Remote Sensing Reviews* 4 (1): 1–212. doi:10.1080/02757258809532105.

Hilker, T., M. A. Wulder, N. C. Coops, J. Linke, J. G. Greg McDermid, F. G. Masek, and J. C. White. 2009a. "A New Data Fusion Model for High Spatial- and Temporal-Resolution Mapping of Forest Disturbance Based on Landsat and MODIS." *Remote Sensing of Environment* 113 (8): 1613–1627. doi:10.1016/j.rse.2009.03.007.

Hilker, T., M. A. Wulder, N. C. Coops, N. Seitz, J. C. White, F. Gao, J. G. Masek, and G. Stenhouse. 2009b. "Generation of Dense Time Series Synthetic Landsat Data through Data Blending with MODIS Using a Spatial and Temporal Adaptive Reflectance Fusion Model." *Remote Sensing of Environment* 113 (9): 1988–1999. doi:10.1016/j.rse.2009.05.011.

Houborg, R., M. F. McCabe, and F. Gao. 2016. "A Spatio-Temporal Enhancement Method for Medium Resolution LAI (STEM-LAI)." *International Journal of Applied Earth Observation and Geoinformation* 47: 15–29. doi:10.1016/j.jag.2015.11.013.

Huang, B., and H. Song. 2012. "Spatiotemporal Reflectance Fusion via Sparse Representation." *IEEE Transactions on Geoscience and Remote Sensing* 50 (10): 3707–3716.

Huang, C., S. N. Goward, J. G. Masek, F. Gao, E. F. Vermote, N. Thomas, K. Schleeweis, R. E. Kennedy, Z. Zhu, J. C. Eidenshink, and J. R. G. Townshend. 2009. "Development of Time Series Stacks of Landsat Images for Reconstructing Forest Disturbance History." *International Journal of Digital Earth* 2 (3): 195–218. doi:10.1080/17538940902801614.

Huang, J., F. Sedano, Y. Huang, M. Hongyuan, L. Xinlu, S. Liang, L. Tian, X. Zhang, J. Fan, and W. Wenbin. 2016. "Assimilating a Synthetic Kalman Filter Leaf Area Index Series into the WOFOST Model to Estimate Regional Winter Wheat Yield." *Agricultural and Forest Meteorology* 216: 188–202. doi:10.1016/j.agrformet.2015.10.013.

Jacquemoud, S., and F. Baret. 1990. "PROSPECT: A Model of Leaf Optical Properties Spectra." *Remote Sensing of Environment* 34 (2): 75–91. doi:10.1016/0034-4257(90)90100-Z.

Jacquemoud, S., F. Baret, B. Andrieu, F. M. Danson, and K. Jaggard. 1995. "Extraction of Vegetation Biophysical Parameters by Inversion of the PROSPECT + SAIL Models on Sugar Beet Canopy Reflectance Data. Application to TM and AVIRIS Sensors." *Remote Sensing of Environment* 52 (3): 163–172. doi:10.1016/0034-4257(95)00018-V.

Jacquemoud, S., S. L. Ustin, J. Verdebout, G. Schmuck, G. Andreoli, and B. Hosgood. 1996. "Estimating Leaf Biochemistry Using the PROSPECT Leaf Optical Properties Model." *Remote Sensing of Environment* 56 (3): 194–202. doi:10.1016/0034-4257(95)00238-3.

Jacquemoud, S., W. Verhoef, F. Baret, P. J. Cédric Bacour, G. P. Zarco-Tejada, C. F. Asner, and S. L. Ustin. 2009. ""PROSPECT+SAIL Models." *A Review of Use for Vegetation Characterization." Remote Sensing of Environment* 113: S56–S66. doi:10.1016/j.rse.2008.01.026.

Ju, J., and D. P. Roy. 2008. "The Availability of Cloud-Free Landsat ETM+ Data over the Conterminous United States and Globally." *Remote Sensing of Environment* 112 (3): 1196–1211. doi:10.1016/j.rse.2007.08.011.

Knyazikhin, Y., J. V. Martonchik, R. B. Myneni, D. J. Diner, and S. W. Running. 1998. "Synergistic Algorithm for Estimating Vegetation Canopy Leaf Area Index and Fraction of Absorbed Photosynthetically Active Radiation from MODIS and MISR Data." *Journal of Geophysical Research: Atmospheres* 103 (D24): 32257–32275. doi:10.1029/98jd02462.

Korhonen, L., P. P. Hadi, and M. Rautiainen. 2017. "Comparison of Sentinel-2 and Landsat 8 in the Estimation of Boreal Forest Canopy Cover and Leaf Area Index." *Remote Sensing of Environment* 195: 259–274. doi:http://dx.doi.org/10.1016/j.rse.2017.03.021.

Li, X., F. Ling, G. M. Foody, G. Yong, Y. Zhang, and D. Yun. 2017a. "Generating a Series of Fine Spatial and Temporal Resolution Land Cover Maps by Fusing Coarse Spatial Resolution Remotely Sensed Images and Fine Spatial Resolution Land Cover Maps." *Remote Sensing of Environment* 196: 293–311. doi:10.1016/j.rse.2017.05.011.

Li, Y., C. Huang, J. Hou, G. Juan, G. Zhu, and L. Xin. 2017b. "Mapping Daily Evapotranspiration Based on Spatiotemporal Fusion of ASTER and MODIS Images over Irrigated Agricultural Areas in the Heihe River Basin, Northwest China." *Agricultural and Forest Meteorology* 244: 82–97. doi:10.1016/j.agrformet.2017.05.023.

Li, Z., H. Tang, X. Xin, B. Zhang, and D. Wang. 2014. "Assessment of the MODIS LAI Product Using Ground Measurement Data and HJ-1A/1B Imagery in the Meadow Steppe of Hulunber, China." *Remote Sensing* 6 (7): 6242. doi:10.3390/rs6076242.

Li, Z., H. Tang, B. Zhang, G. Yang, and X. Xin. 2015. "Evaluation and Intercomparison of MODIS and GEOV1 Global Leaf Area Index Products over Four Sites in North China." *Sensors* 15 (3): 6196. doi:10.3390/s150306196.

Li, Z., J. Wang, H. Tang, C. Huang, F. Yang, B. Chen, X. Wang, X. Xin, and G. Yong. 2016. "Predicting Grassland Leaf Area Index in the Meadow Steppes of Northern China: A Comparative Study of Regression Approaches and Hybrid Geostatistical Methods." *Remote Sensing* 8 (8): 632. doi:10.3390/rs8080632.

Martin Enrique, R.-S., R. Ponce-Hernandez, S. E. Franklin, and C. A. Aguirre-Salado. 2015. "Comparison of Data Gap-Filling Methods for Landsat ETM+ SLC-off Imagery for Monitoring Forest Degradation in a Semi-Deciduous Tropical Forest in Mexico." *International Journal of Remote Sensing* 36 (11): 2786–2799. doi:10.1080/01431161.2015.1047991.

Masek, J. G., E. F. Vermote, N. E. Saleous, R. Wolfe, F. G. Hall, K. F. Huemmrich, G. Feng, J. Kutler, and L. Teng-Kui. 2006. "A Landsat Surface Reflectance Dataset for North America, 19902000." *IEEE Geoscience and Remote Sensing Letters* 3 (1): 68–72. doi:10.1109/lgrs.2005.857030.

Mingquan, W., Z. Niu, C. Wang, W. Chaoyang, and L. Wang. 2012. "Use of MODIS and Landsat Time Series Data to Generate High-Resolution Temporal Synthetic Landsat Data Using a Spatial and Temporal Reflectance Fusion Model."." *Journal of Applied Remote Sensing* 6 (1): 1–13.

Myneni, R. B., S. Hoffman, Y. Knyazikhin, J. L. Privette, J. Glassy, Y. Tian, Y. Wang, et al. 2002. "Global Products of Vegetation Leaf Area and Fraction Absorbed PAR from Year One of MODIS Data." *Remote Sensing of Environment* 83 (1): 214–231. doi:10.1016/S0034-4257(02)00074-3.

Pasolli, L., S. Asam, M. Castelli, L. Bruzzone, G. Wohlfahrt, M. Zebisch, and C. Notarnicola. 2015. "Retrieval of Leaf Area Index in Mountain Grasslands in the Alps from MODIS Satellite Imagery." *Remote Sensing of Environment* 165: 159–174. doi:10.1016/j.rse.2015.04.027.

Pinty, B., N. Gobron, S. A. Jean-Luc Widlowski, W. Gerstl, M. M. Verstraete, M. Antunes, C. Bacour, et al. 2001. "Radiation Transfer Model Intercomparison (RAMI) Exercise." *Journal of Geophysical Research: Atmospheres* 106 (D11): 11937–11956. doi:10.1029/2000jd900493.

Rao, Y., X. Zhu, J. Chen, and J. Wang. 2015. "An Improved Method for Producing High Spatial-Resolution NDVI Time Series Datasets with Multi-Temporal MODIS NDVI Data and Landsat TM/ETM+ Images." *Remote Sensing* 7 (6): 7865. doi:10.3390/rs70607865.

Roerink, G. J., M. Menenti, and W. Verhoef. 2000. "Reconstructing Cloudfree NDVI Composites Using Fourier Analysis of Time Series." *International Journal of Remote Sensing* 21 (9): 1911–1917. doi:10.1080/014311600209814.

Rossello, P., and F. Baret. 2007. "Validation of Land European Remote Sensing Instruments." http://w3.avignon.inra.fr/valeri/Meeting_Reports/Davos_2007/Rossello_Davos_VALERI.pdf.

Running, S. W., and J. C. Coughlan. 1988. "A General Model of Forest Ecosystem Processes for Regional Applications I. Hydrologic Balance, Canopy Gas Exchange and Primary Production Processes." *Ecological Modelling* 42 (2): 125–154. doi:10.1016/0304-3800(88)90112-3.

Running, S. W., R. R. Nemani, D. L. Peterson, L. E. Band, D. F. Potts, L. L. Pierce, and M. A. Spanner. 1989. "Mapping Regional Forest Evapotranspiration and Photosynthesis by Coupling Satellite Data with Ecosystem Simulation." *Ecology* 70 (4): 1090–1101. doi:10.2307/1941378.

Running, S. W., D. D. Baldocchi, D. P. Turner, S. T. Gower, P. S. Bakwin, and K. A. Hibbard. 1999. "A Global Terrestrial Monitoring Network Integrating Tower Fluxes, Flask Sampling, Ecosystem Modeling and EOS Satellite Data." *Remote Sensing of Environment* 70 (1): 108–127. doi:10.1016/S0034-4257(99)00061-9.

Savitzky, A., and M. J. E. Golay. 1964. "Smoothing and Differentiation of Data by Simplified Least Squares Procedures." *Analytical Chemistry* 36 (8): 1627–1639. doi:10.1021/ac60214a047.

Schaaf, C., and Z. Wang 2015. "MCD43A4 MODIS/Terra+Aqua BRDF/Albedo Nadir BRDF Adjusted RefDaily L3 Global - 500m V006: Distributed by NASA EOSDIS Land Processes DAAC." doi:10.5067/MODIS/MCD43A4.006

Schaepman-Strub, G., M. E. Schaepman, T. H. Painter, S. Dangel, and J. V. Martonchik. 2006. "Reflectance Quantities in Optical Remote sensing—Definitions and Case Studies." *Remote Sensing of Environment* 103 (1): 27–42. doi:10.1016/j.rse.2006.03.002.

Sedano, F., P. Kempeneers, and G. Hurtt. 2014. "A Kalman Filter-Based Method to Generate Continuous Time Series of Medium-Resolution NDVI Images." *Remote Sensing* 6 (12): 12381–12408. doi:10.3390/rs61212381.

Sellers, P., and D. Schimel. 1993. "Remote Sensing of the Land Biosphere and Biogeochemistry in the EOS Era: Science Priorities, Methods and implementation—EOS Land Biosphere and Biogeochemical Cycles Panels." *Global and Planetary Change* 7 (4): 279–297. doi:10.1016/0921-8181(93)90002-6.

Si, Y., M. Schlerf, R. Zurita-Milla, A. Skidmore, and T. Wang. 2012. "Mapping Spatio-Temporal Variation of Grassland Quantity and Quality Using MERIS Data and the PROSAIL Model." *Remote Sensing of Environment* 121: 415–425. doi:10.1016/j.rse.2012.02.011.

Sun, L., M. C. Anderson, F. Gao, C. Hain, J. G. Alfieri, A. Sharifi, G. W. McCarty, Y. Yang, W. P. Kustas, and L. McKee. 2017. "Investigating Water Use over the Choptank River Watershed Using a Multisatellite Data Fusion Approach." *Water Resources Research* 53 (7): 5298–5319. doi:10.1002/2017wr020700.

Tang, H., W. Gao, X. Lijun, R. Yan, B. Chen, and X. Xin. 2015a. "Monitoring Forage Harvesting Area in Semi-Arid Pasture Based on Landsat TM Images." *Transactions of the Chinese Society of Agricultural Engineering* 31 (23): 160–167.

Tang, H., L. Zhenwang, Z. Zhu, B. Chen, B. Zhang, and X. Xin. 2015b. "Variability and Climate Change Trend in Vegetation Phenology of Recent Decades in the Greater Khingan Mountain Area, Northeastern China." *Remote Sensing* 7 (9): 11914. doi:10.3390/rs70911914.

Tao, X., S. Liang, H. Tao, and H. Jin. 2016. "Estimation of Fraction of Absorbed Photosynthetically Active Radiation from Multiple Satellite Data: Model Development and Validation." *Remote Sensing of Environment* 184 (Supplement C): 539–557. doi:10.1016/j.rse.2016.07.036.

Verhoef, W. 1984. "Light Scattering by Leaf Layers with Application to Canopy Reflectance Modeling: The SAIL Model." *Remote Sensing of Environment* 16 (2): 125–141. doi:10.1016/0034-4257(84)90057-9.

Verhoef, W. 1985. "Earth Observation Modeling Based on Layer Scattering Matrices." *Remote Sensing of Environment* 17 (2): 165–178. doi:10.1016/0034-4257(85)90072-0.

Verhoef, W., L. Jia, Q. Xiao, and Z. Su. 2007. "Unified Optical-Thermal Four-Stream Radiative Transfer Theory for Homogeneous Vegetation Canopies." *IEEE Transactions on Geoscience and Remote Sensing* 45 (6): 1808–1822. doi:10.1109/tgrs.2007.895844.

Vermote, E., C. Justice, M. Claverie, and B. Franch. 2016. "Preliminary Analysis of the Performance of the Landsat 8/OLI Land Surface Reflectance Product." *Remote Sensing of Environment* 185: 46–56. doi:10.1016/j.rse.2016.04.008.

Verrelst, J., M. E. Schaepman, B. Koetz, and M. Kneubühler. 2008. "Angular Sensitivity Analysis of Vegetation Indices Derived from CHRIS/PROBA Data." *Remote Sensing of Environment* 112 (5): 2341–2353. doi:10.1016/j.rse.2007.11.001.

Verrelst, J., G. Camps-Valls, J. Muñoz-Marí, J. P. Rivera, J. G. Frank Veroustraete, P. W. Clevers, and J. Moreno. 2015. "Optical Remote Sensing and the Retrieval of Terrestrial Vegetation Bio-Geophysical Properties – A Review." *ISPRS Journal of Photogrammetry and Remote Sensing* 108: 273–290. doi:10.1016/j.isprsjprs.2015.05.005.

Verrelst, J., E. Romijn, and L. Kooistra. 2012. "Mapping Vegetation Density in a Heterogeneous River Floodplain Ecosystem Using Pointable CHRIS/PROBA Data." *Remote Sensing* 4 (9): 2866. doi:10.3390/rs4092866.

Verrelst, J., M. E. Schaepman, Z. Malenovský, and G. P. W. Jan Clevers. 2010. "Effects of Woody Elements on Simulated Canopy Reflectance: Implications for Forest Chlorophyll Content Retrieval." *Remote Sensing of Environment* 114 (3): 647–656. doi:10.1016/j.rse.2009.11.004.

Wang, P., F. Gao, and J. G. Masek. 2014. "Operational Data Fusion Framework for Building Frequent Landsat-Like Imagery." *IEEE Transactions on Geoscience and Remote Sensing* 52 (11): 7353–7365. doi:10.1109/tgrs.2014.2311445.

Weiss, M., and F. Baret. 1999. "Evaluation of Canopy Biophysical Variable Retrieval Performances from the Accumulation of Large Swath Satellite Data." *Remote Sensing of Environment* 70 (3): 293–306. doi:10.1016/S0034-4257(99)00045-0.

Weng, Q., F. Peng, and F. Gao. 2014. "Generating Daily Land Surface Temperature at Landsat Resolution by Fusing Landsat and MODIS Data." *Remote Sensing of Environment* 145: 55–67. doi:10.1016/j.rse.2014.02.003.

West, N. E., and M. A. Hassan. 1985. "Recovery of Sagebrush-Grass Vegetation following Wildfire." *Journal of Range Management* 38 (2): 131–134. doi:10.2307/3899255.

Wiegand, C. L., A. J. Richardson, and E. T. Kanemasu. 1979. "Leaf Area Index Estimates for Wheat from LANDSAT and Their Implications for Evapotranspiration and Crop Modeling1." *Agronomy Journal* 71 (2): 336–342. doi:10.2134/agronj1979.00021962007100020027x.

Wu, Q., Y. Jin, Y. Bao, Q. Hai, R. Yan, B. Chen, H. Zhang, et al. 2015. "Comparison of Two Inversion Methods for Leaf Area Index Using HJ-1 Satellite Data in a Temperate Meadow Steppe." *International Journal of Remote Sensing* 1–16. doi:10.1080/01431161.2015.1040135.

Wulder, M. A., J. G. Masek, W. B. Cohen, T. R. Loveland, and C. E. Woodcock. 2012. "Opening the Archive: How Free Data Has Enabled the Science and Monitoring Promise of Landsat." *Remote Sensing of Environment* 122: 2–10. doi:10.1016/j.rse.2012.01.010.

Xiao, X., B. Braswell, Q. Zhang, S. Boles, S. Frolking, and B. Moore. 2003. "Sensitivity of Vegetation Indices to Atmospheric Aerosols: Continental-Scale Observations in Northern Asia." *Remote Sensing of Environment* 84 (3): 385–392. doi:10.1016/S0034-4257(02)00129-3.

Yan, K., T. Park, G. Yan, C. Chen, B. Yang, Z. Liu, R. Nemani, Y. Knyazikhin, and R. Myneni. 2016a. "Evaluation of MODIS LAI/FPAR Product Collection 6. Part 1: Consistency and Improvements." *Remote Sensing* 8 (5): 359.

Yan, K., T. Park, G. Yan, Z. Liu, B. Yang, C. Chen, R. Nemani, Y. Knyazikhin, and R. Myneni. 2016b. "Evaluation of MODIS LAI/FPAR Product Collection 6. Part 2: Validation and Intercomparison." *Remote Sensing* 8 (6): 460. doi:10.3390/rs8060460.

Yang, W., D. Huang, J. C. Bin Tan, N. V. Stroeve, S. Y. Knyazikhin, R. R. Nemani, and R. B. Myneni. 2006. "Analysis of Leaf Area Index and Fraction of PAR Absorbed by Vegetation Products from the Terra MODIS Sensor: 20002005." *IEEE Transactions on Geoscience and Remote Sensing* 44 (7): 1829–1842. doi:10.1109/tgrs.2006.871214.

Yang, Y., M. C. Anderson, F. Gao, C. R. Hain, K. A. Semmens, W. P. Kustas, A. Noormets, R. H. Wynne, V. A. Thomas, and G. Sun. 2017. "Daily Landsat-Scale Evapotranspiration Estimation over a Forested Landscape in North Carolina, USA, Using Multi-Satellite Data Fusion." *Hydrology and Earth System Sciences* 21 (2): 1017. doi:10.5194/hess-21-1017-2017.

Yin, G., L. Ainong, H. Jin, W. Zhao, J. Bian, Q. Yonghua, Y. Zeng, and X. Baodong. 2017. "Derivation of Temporally Continuous LAI Reference Maps through Combining the LAINet Observation System with CACAO." *Agricultural and Forest Meteorology* 233 (Supplement C): 209–221. doi:10.1016/j.agrformet.2016.11.267.

Zhu, X., J. Chen, F. Gao, X. Chen, and J. G. Masek. 2010. "An Enhanced Spatial and Temporal Adaptive Reflectance Fusion Model for Complex Heterogeneous Regions." *Remote Sensing of Environment* 114 (11): 2610–2623. doi:10.1016/j.rse.2010.05.032.

Zhu, X., E. H. Helmer, F. Gao, D. Liu, J. Chen, and M. A. Lefsky. 2016. "A Flexible Spatiotemporal Method for Fusing Satellite Images with Different Resolutions." *Remote Sensing of Environment* 172: 165–177. doi:10.1016/j.rse.2015.11.016.

Zhu, X., D. Liu, and J. Chen. 2012. "A New Geostatistical Approach for Filling Gaps in Landsat ETM+ SLC-off Images." *Remote Sensing of Environment* 124: 49–60.